The EUMETSAT Satellite Application Facility on Land Surface Analysis (LSA SAF)

Product User Manual

Land Surface Albedo

PRODUCTS: LSA-01 (MDAL), LSA-02 (MTAL)



Reference Number: SAF/LAND/MF/PUM_Al/1.5
Issue/Revision Index: Issue 1.5
Last Change: 19/03/2010

DOCUMENT SIGNATURE TABLE

	Name	Date	Signature
Prepared by :	**Météo-France / CNRM**	**19/03/2010**	
Approved by :	**Land SAF Project Manager**	**19/03/2010**	

DOCUMENTATION CHANGE RECORD

Issue / Revision	Date	Description:
Version 0.0	**29/10/2004**	**Preliminary version**
Version 1.0	**02/11/2004**	**Version prepared for SIVVRR 2**
Version 1.1	**08/03/2005**	**Version prepared for Check-Point Meeting**
Version 1.2	**01/06/2005**	**Version prepared for ORR-1**
Version 1.3	**20/01/2006**	**Version prepared for ORR-1 Close-Out**
Version 1.4	**19/10/2006**	**Version prepared for OR-1**
Version 1.5	**19/03/2010**	**Version prepared for ORR-A**

DISTRIBUTION LIST

Internal Consortium Distribution		
Organisation	**Name**	**No. Copies**
IM	Pedro Viterbo	
IM	Luís Pessanha	
IM	Isabel Trigo	
IDL	Carlos da Camara	
IM	Isabel Monteiro	
IM	Sandra Coelho	
IM	Carla Barroso	
IM	Pedro Diegues	
IM	Teresa Calado	
IM	Benvinda Barbosa	
IM	Ana Veloso	
IMK	Folke-S. Olesen	
IMK	Frank Goettsche	
IMK	Ewa Kabsch	
MF	Jean-Louis Roujean	
MF	Olivier Hautecoeu	
MF	Dominique Carrer	
RMI	Françoise Meulenberghs	
RMI	Arboleda Alirio	
RMI	Nicolas Ghilain	
FMI	Niilo Siljamo	
UV	Joaquin Melia	
UV	F. Javier García Haro	
UV/EOLAB	Fernando Camacho	
UV	Aleixander Verger	

External Distribution		
Organisation	**Name**	**No. Copies**
EUMETSAT	Frédéric Gasiglia	
EUMETSAT	Dominique Faucher	
EUMETSAT	Lorenzo Sarlo	
EUMETSAT	Lothar Schueller	
EDISOFT	Teresa Cardoso	
EDISOFT	Carlos Vicente	
EDISOFT	Cleber Balan	
SKYSOFT	Rui Alves	

SKYSOFT	**João Canário**	

Steering Group Distribution		
Nominated by:	**Name**	**No. Copies**
IM	**Carlos Direitinho Tavares**	
EUMETSAT	**Lorenzo Sarlo**	
EUMETSAT	**Yves Govaerts**	
EUMETSAT	**François Montagner**	
STG/AFG (USAM)	**Luigi de Leonibus**	
MF	**François Bouyssel**	
RMI	**Steven Dewitte**	
FMI	**Carl Fortelius**	

Table of Contents

1 INTRODUCTION 10
2 ALGORITHM 15
2.1 Overview 15
2.2 Albedo Definition 18
2.3 Atmospheric Correction 21
2.4 Model Inversion 22
2.5 Surface BRDF Model 25
2.6 Weighting of Measurements 26
2.7 Illustration of the Model Inversion 28
2.8 Temporal Composition 29
2.9 Angular Integration 31
2.10 Narrow- to Broad-band Conversion 33
2.11 Signification of the Uncertainty Estimates 35
3 PRODUCT DESCRIPTION 36
3.1 Overview 36
3.2 Geolocation / Rectification 36
3.3 File Formats 36
3.4 Product Content 39
3.5 Summary of Product Characteristics 42
4 VALIDATION 44
4.1 Comparison with the MODIS Albedo Product 44
4.2 Known Problems and Limitations 45
4.3 Comparison between D01 and D10 products 45
5 REFERENCES 47

List of Figures

Figure 1 - The LSA SAF geographical areas for SEVIRI-based products.....13

Figure 2: Flow chart of the algorithm for atmospheric correction, BRDF model inversion, and albedo determination.....17

Figure 3: Illumination (left) and observation (right) geometries corresponding to a geographical location of [47° 47' N, 10° 37' E] and an observation period between the days of year 150 and 170. The relative azimuth angle ϕ is identical for the two graphs. The convention was chosen such that the top of the graphs (ϕ=0°) corresponds to the backscattering regime. The colours of the dots denote observations taken by different sensors as follows: Red: SEVIRI/MSG, Green: AVHRR/METOP, Blue: AVHRR/NOAA. 22

Figure 4: Angular dependence of the "geometric" (left) and "volume scattering" (right) kernels of the reflectance model introduced by Roujean et al. (1992). In the graphs negative zenith angle values correspond to the backscatter direction (relative azimuth angle ϕ=0°) and positive zenith angle values to the forward scatter direction (ϕ=180°). 26

Figure 5: Example for the results of the TOC-reflectance model inversion in the three used SEVIRI channels (49.02°N, 2.53°E; 1st of July 2006). Negative values of the solar zenith angles correspond to observations acquired before local solar noon. 28

Figure 6: The dependence of the 0.8µm-channel reflectance factor on the direction of the outgoing light ray for different incidence directions according to the model fit of the example case from Figure 5. 29

Figure 7: Effective temporal weight function in the recursive composition scheme. The characteristic time scale is τ = 5 days.....30

Figure 8: Illumination zenith angle dependence of the directional-hemispherical kernel integrals for the Roujean et al. (1992) model.....31

Figure 9: Dependence of the directional-hemispherical albedo on the illumination zenith angle for the example case from Figure 5. The value at the reference angle θ_{ref} as well as the bi-hemispherical estimate are indicated. 32

Figure 10: Broad-band albedo product for the 1st of March 2006. The top left panel shows the total broad-band directional-hemispherical albedo, the top right panel the corresponding uncertainty estimate, and the bottom left panel the quality flag. For the latter the legend indicates which bits were used for the visualisation, e.g. "……00" signifies that pixels with bits 0 and 1 equal to zero are depicted in dark blue colour. The bottom right panel shows the "age" of the last available observation used for each image pixel. 40

Figure 11: Colour composite derived from the three spectral directional-hemispherical albedo estimates for the 1st of March 2006.....41

Figure 12: Temporal evolution (June 2005 to September 2006) of the bias and standard deviation between LSA SAF and MODIS broad-band albedo results for Europe. The position of the symbols in the graphs indicates the bias, and the length of the bars (from the centre to each end) corresponds to the standard deviation. Top Left: Total short-wave bi-hemispherical. Top Right: Total short-wave directional-hemispherical. Bottom Left: Visible directional-hemispherical. Bottom Right: Near infrared directional-hemispherical. 45

Figure 13: Time series of broadband albedo acquired in 2009 over 2 confident sites (Top: Gobabeb; Bottom: Toravere). Ground measurements (orange). D01 (black). D30 (red). Red/blue dots on the X-axis indicate missing data. 48

List of Tables

Table 1: Summary of LSA SAF operational or under-development products. Temporal resolution specifies the time interval to which the product applies. ...11

Table 2: Product Requirements for AL, in terms of area coverage, resolution and accuracy. 15

Table 3: Coefficients for the parameterisation of the TOC reflectance factor uncertainty estimates....28

Table 4: N arrow- to broad-band conversion coefficients for the SEVIRI channels (van Leeuwen and Roujean, 2002). 34

Table 5: Narrow- to broad-band conversion coefficients for pixels flagged as snow-covered calculated with tools developed by Samain (2005)……..34

Table 6: Characteristics of the four LSA SAF geographical areas: Each region is defined by the corner positions relative to an MSG image of 3712 columns per 3712 lines with indices starting at 1 in the North and West. 36

Table 7: Maximum values for number of columns (ncol) and lines (nlin), for each Land-SAF geographical area, and the respective COFF and LOFF coefficients needed to geo-locate the data. 40

Table 8: Content of the broad-band surface albedo product files. 41

Table 9: Content of the spectral surface albedo product files for each channel β …43

Table 10: Albedo product quality flag information. 44

Table 11: General HDF5 attributes. 53

Table 12: Dataset attributes....56

1 Introduction

The EUMETSAT Satellite Application Facility (SAF) on Land Surface Analysis (LSA; Trigo et al., 2010) is part of the SAF Network, a set of specialised development and processing centres, serving as EUMETSAT (European organization for the Exploitation of Meteorological Satellites) distributed Applications Ground Segment. The SAF network complements the product-oriented activities at the EUMETSAT Central Facility in Darmstadt. The main purpose of the LSA SAF is to take full advantage of remotely sensed data, particularly those available from EUMETSAT sensors, to measure land surface variables, which will find primarily applications in meteorology (http://landsaf.meteo.pt/).

The spin-stabilised Meteosat Second Generation (MSG) has an imaging-repeat cycle of 15 minutes. The Spinning Enhanced Visible and Infrared Imager (SEVIRI) radiometer embarked on the MSG platform encompasses unique spectral characteristics and accuracy, with a 3 km resolution (sampling distance) at nadir (1km for the high-resolution visible channel), and 12 spectral channels (Schmetz et al., 2002).

The EUMETSAT Polar System (EPS) is Europe's first polar orbiting operational meteorological satellite and the European contribution to a joint polar system with the U.S. EUMETSAT will have the operational responsibility for the "morning orbit" with Meteorological-Operational (Metop) satellites, the first of which was successfully launched on October 19, 2006. Despite the wide range of sensors on-board Metop (http://www.eumetsat.int/), most LSA SAF parameters make use of the Advanced Very High Resolution Radiometer (AVHRR) and, to a lesser extent, of the Advanced Scatterometer (ASCAT).

Several studies have stressed the role of land surface processes on weather forecasting and climate modelling (e.g., Dickinson et al., 1983; Mitchell et al., 2004; Ferranti and Viterbo, 2006). The LSA SAF has been especially designed to serve the needs of the meteorological community, particularly Numerical Weather Prediction (NWP). However, there is no doubt that the LSA SAF addresses a much broader community, which includes users from:

- Weather forecasting and climate modelling, requiring detailed information on the nature and properties of land.
- Environmental management and land use, needing information on land cover type and land cover changes (e.g. provided by biophysical parameters or thermal characteristics).

- Agricultural and Forestry applications, requiring information on incoming/outgoing radiation and vegetation properties.
- Renewable energy resources assessment, particularly biomass, depending on biophysical parameters, and solar energy.
- Natural hazards management, requiring frequent observations of terrestrial surfaces in both the solar and thermal bands.
- Climatological applications and climate change detection, requiring long and homogeneous time-series.

Table 1 Summary of LSA SAF operational or under-development products. Temporal resolution specifies the time interval to which the product applies.

	Product	Spatial Coverage	Temporal Resolution
Surface Radiation Budget	AL – Albedo	MSG disk	5-day & 30-day
	LST – Land Surface Temperature	MSG disk / Global*	Instantaneous
	EM – Emissivity	MSG disk / Global*	5-day & 30-day
	DSSF – Down-welling Surface Short-wave Flux	MSG disk / Global*	Instantaneous & Daily
	DSLF – Down-welling Surface Long-wave Flux	MSG disk / Global*	Instantaneous & Daily
Biogeophysical Parameters I	SC – Snow Cover	MSG disk / Global	Daily
	ET – Evapotranspiration	MSG disk	Daily / 30 min
Biogeophysical Parameters II	FVC – Fraction of Vegetation Cover	MSG disk / Global*	5-day & 30-day
	LAI – Leaf Area Index	MSG disk / Global*	5-day & 30-day

	FAPAR – Fraction of Absorbed Photosynthetic Active Radiation	MSG disk / Global*	5-day & 30-day
	RFM – Risk of Fire Mapping	Europe	Daily
	FD&M – Fire Detection & Monitoring	MSG disk	15-min & Daily
	FRP – Fire Radiative Power	MSG disk	15-min & hourly

*Global and 12-hourly products refer to retrievals from AVHRR/EPS.
**Indirectly, via other LSA SAF components (AL, DSSF, DSLF, FVC, LAI, …)
***For cloud identification and classification.

The LSA SAF products (Table 1) are based on level 1.5 SEVIRI/Meteosat and/or level 1b Metop data. Forecasts provided by the European Centre for Medium-range Weather Forecasts (ECMWF) are also used as ancillary data for atmospheric correction.
Most products derived from SEVIRI/Meteosat are generated at full spatial resolution (3km pixel sampling distance at nadir), for 4 different geographical areas within Meteosat disk (Figure 1):

- Euro – Europe, covering all EUMETSAT member states;
- NAfr – Northern Africa encompassing the Sahara and Sahel regions, and part of equatorial Africa.
- SAfr – Southern Africa covering the African continent south of the Equator.
- SAme – South American continent within the Meteosat disk.

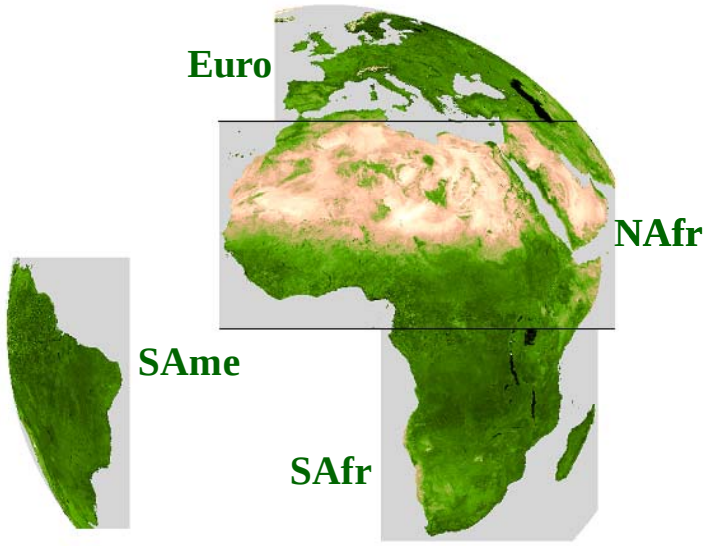


Figure 1 - The LSA SAF geographical areas for SEVIRI-based products.

Metop derived parameters are available at level 1b full spatial resolution and for the processed Product Distribution Units (PDUs), each corresponding to about 3 minutes of instrument-specific observation data. Composite and re-projected products shall also be available.
All LSA SAF products are validated regularly against ground measurements, model outputs, or similar parameters retrieved from other sensors, as appropriate.

Furthermore, each retrieved value is distributed with a quality flag and/or error bar providing a qualitative/quantitative measure of the expected accuracy.
The LSA SAF products are currently available from LSA SAF website (http://landsaf.meteo.pt) that contains real time examples of the products as well as updated information.
This document is one of the product manuals dedicated to LSA SAF users. The algorithm and the main characteristics of the Land Surface Albedo (AL) generated by the LSA SAF from SEVIRI and AVHRR data system are described in the following sections. The characteristics of AVHRR and SEVIRI based AL products provided by the LSA SAF are described in Table 2. Further details on the LSA SAF product requirements may be found in the Product Requirements Document (PRD) available at the LSA SAF website http://landsaf.meteo.pt).

Table 2 Product Requirements for AL, in terms of area coverage, resolution and accuracy.

DSSF Product	Product Identifier	Coverage	Resolution		Accuracy		
			Temporal	Spatial	Threshold	Target	Optimal
MDAL: AL_SEVIRI	LSA-01	MSG disk	1 day	MSG pixel resolution	20%	AL>0.15: 20% AL<0.15: 0.03	7.5%
MTAL: AL_SEVIRI	LSA-02	MSG disk	10-day	MSG pixel resolution °	20%	AL>0.15: 10% AL<0.15: 0.015	5%

2 Algorithm

2.1 Overview

Land surface albedo quantifies the fraction of energy reflected by the surface of the Earth. As a corollary it then also determines the fraction of energy absorbed by the surface and transformed into heat or latent energy. Land surface albedo therefore is a key variable for characterising the energy balance in the coupled surface-atmosphere system and constitutes an indispensable input quantity for soil-vegetation-atmosphere transfer models.

Owing to strong feedback effects, the knowledge of surface albedo is also important for determining atmospheric conditions in the boundary layer. As Numerical Weather Prediction models become more sophisticated, it will become increasingly important to accurately describe the spatial and temporal albedo variations. On longer timescales, studies carried out with Global Circulation Models have revealed the sensitivity of climate with respect to changes in surface albedo.

The largest surface albedo changes are caused by snow fall. Snow characteristics and duration of snow cover have a direct impact on the environmental system. The seasonal monitoring of snow therefore is an important subject for numerical weather prediction, climate studies, and hydrology. Snow albedo varies with environmental conditions, land cover, and snow metamorphism. One of the objectives of the delivered product is to quantify the albedo changes on small timescales.

The most relevant albedo quantity for applications related to the energy budget refers to the total short-wave broad-band interval comprising the visible and near infrared wavelength ranges where the solar down-welling radiation dominates. In more refined models the albedo values in the visible and near infrared broad-band ranges may also be exploited separately. Estimates for the normalised the LSA SAF algorithm also delivers reflectance factor values and the spectral albedo in the satellite instrument channels. In addition to serving as an intermediate product for deriving the broad-band albedo quantities, the spectral estimates contain a wealth of information about the physical state of the surface. This information can be used for a variety of purposes such as vegetation monitoring and land cover classification, which in turn also constitute important elements for setting up adequate surface modelling schemes.

A well-established approach for operational albedo determination is based on semi-empirical BRDF kernel models which have received a great deal of attention and effort from the optical remote sensing community in the last decades (Roujean et al., 1992; Barnsley et al., 1994; Wanner et al., 1995; Strahler, 1994; Hu et al., 1997). The approach is based on a decomposition of the bi-directional reflectance factor into a number of geometric kernel functions which are associated to the dominant

light scattering processes, e.g. geometric and volumetric effects, a separation between the soil and vegetation, or the conjunction between media which are optically thick and thin (Lucht and Roujean, 2000). Both in situ measurements and numerical experiments have supported this assumption and the use of kernel-based models is widely accepted since they yield a pragmatic and cost-effective solution to the problem of BRDF inversion. For a number of space-borne sensors of the current generation of multi-angular systems the kernel-based approach was adopted for the development of albedo products. These include POLDER, SeaWiFS, VEGETATION, and MODIS (e.g., Leroy et al., 1997; Justice et al., 1998; Wanner et al., 1997; Strahler et al., 1999). On the other hand, different parameterised models and a simultaneous modelling of atmosphere and surface properties were considered for MISR (Diner et al., 1998) and Meteosat (Pinty et al., 2000a-b). The common feature of these algorithms is the correction and exploitation of the variations in sun-sensor geometry that occur as a function of satellite orbit, sensor design, geographical position of the target, and time of the year.

The operational processing scheme of the LSA SAF albedo algorithm is depicted in the flow chart of Figure 2 and comprises four successive steps: First the measured top-of-atmosphere (TOA) radiances delivered by the satellite instrument are corrected for atmospheric effects in order to convert them into the corresponding top-of-canopy (TOC) reflectance values. The spectral TOC-reflectances then serve as the input quantities for the inversion of a linear kernel-driven BRDF model, which allows us to take into account the angular dependence of the reflectance factor. Spectral albedo values in the instrument channels are determined from the angular integrals of the model functions with the retrieved parameter values. Finally, a narrow- to broad-band conversion is performed with a linear regression formula.

Technically the processing chain comprises two distinct modules - one for atmospheric correction and one for model inversion and directional and spectral integration. The atmospheric correction module is applied separately on each SEVIRI image available at intervals of 15 minutes directly after acquisition. The inversion and albedo calculation module, on the other hand, operates on a set of TOC-reflectance images collected during one day. By using the previous inversion result as a priori information, a recursive temporal composition of the information over a longer time period can be achieved in order to guarantee the coherence and spatial completeness of the product.

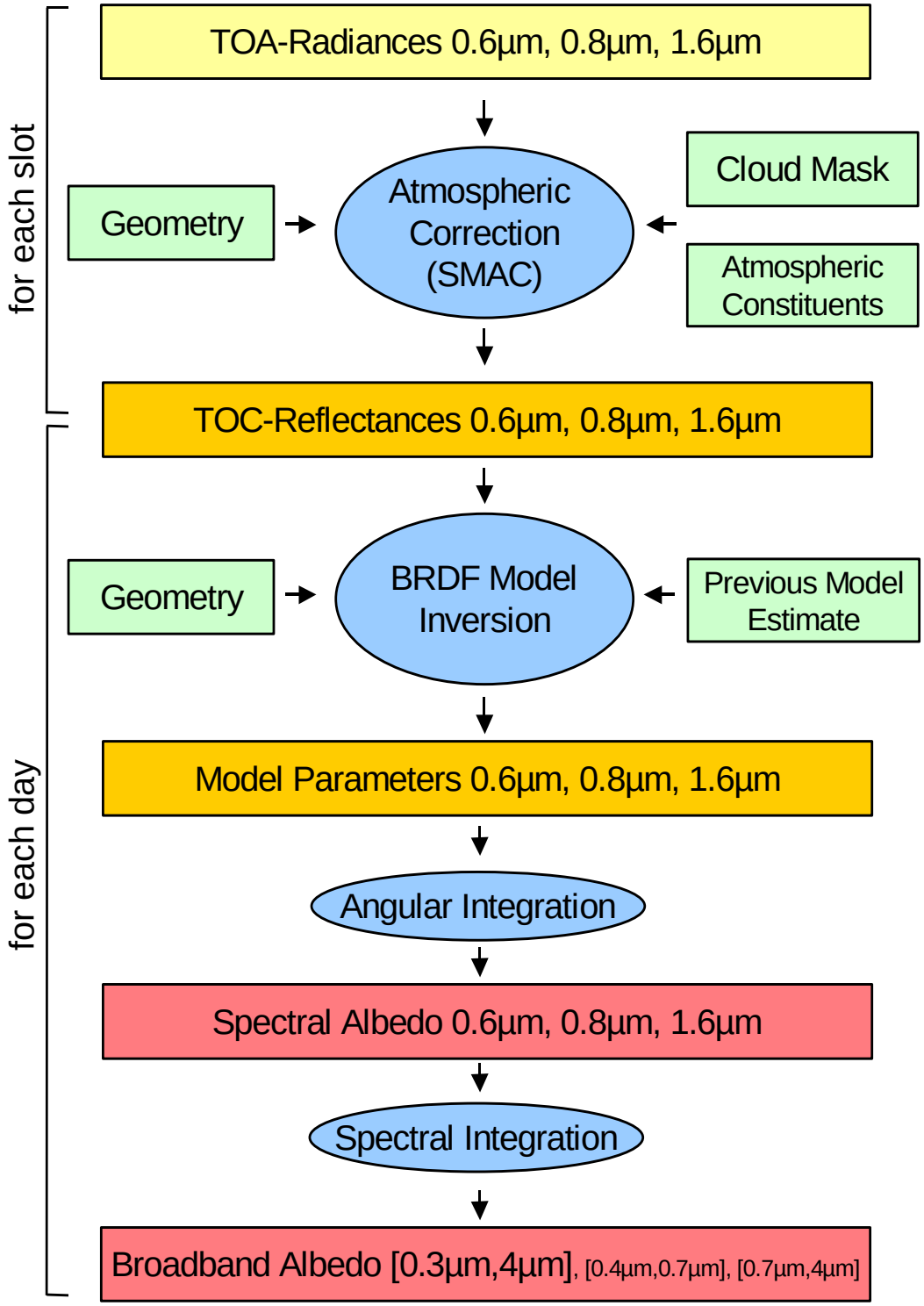


Figure 2: Flow chart of the algorithm for atmospheric correction, BRDF model inversion, and albedo determination.

2.2 Albedo Definition

The spectral albedo of a plane surface is defined as the ratio between the hemispherical integrals of the up-welling (reflected) spectral radiance $L^{\uparrow}(\lambda,\theta_{out},\phi_{out})$ and the down-welling spectral radiance $L^{\downarrow}(\lambda,\theta_{in},\phi_{in})$ weighted by the cosine of the angle between the respective reference direction and the surface normal:

$$a(\lambda) := \frac{\int_{2\pi} L^{\uparrow}(\lambda,\theta_{out},\phi_{out})\cos\theta_{out}\ d\Omega_{out}}{\int_{2\pi} L^{\downarrow}(\lambda,\theta_{in},\phi_{in})\cos\theta_{in}\ d\Omega_{in}}\ , \qquad (1)$$

where $d\Omega_{out} = \sin\theta_{out} d\theta_{out} d\phi_{out}$ and $d\Omega_{in} = \sin\theta_{in} d\theta_{in} d\phi_{in}$. The expression in the denominator defines the spectral irradiance $E^{\downarrow}(\lambda)$. By introducing the bi-directional reflectance factor R, the up-welling radiance distribution can be expressed in terms of the down-welling radiation as

$$L^{\uparrow}(\lambda,\theta_{out},\phi_{out}) = \frac{1}{\pi}\int_{2\pi} R(\lambda,\theta_{out},\phi_{out},\theta_{in},\phi_{in}) L^{\downarrow}(\lambda,\theta_{in},\phi_{in})\cos\theta_{in}\ d\Omega_{in} \qquad (2)$$

and Equation (1) becomes

$$a(\lambda) = \frac{\frac{1}{\pi}\int_{2\pi}\int_{2\pi} R(\lambda,\theta_{out},\phi_{out},\theta_{in},\phi_{in}) L^{\downarrow}(\lambda,\theta_{in},\phi_{in})\cos\theta_{in}\cos\theta_{out}\ d\Omega_{in} d\Omega_{out}}{E^{\downarrow}(\lambda)}\ . \qquad (3)$$

From the result it can be seen that in general the spectral albedo of non-Lambertian surfaces depends on the angular distribution of the incident radiation - which in turn depends on the concentration and properties of scattering agents (e.g. aerosols) in the atmosphere and in particular on the presence of clouds. Therefore the spectral albedo is not a true surface property but rather a characteristics of the coupled surface-atmosphere system.

In the idealised case of purely direct illumination at incidence angles (θ_{dh},ϕ_{dh}), the down-welling radiance is given by $L^{\downarrow}(\lambda,\theta_{in},\phi_{in}) = (\sin\theta_{dh})^{-1}\,\delta(\theta_{in}-\theta_{dh},\phi_{in}-\phi_{dh})E_0(\lambda)$, which results in $E^{\downarrow}(\lambda) = E_0(\lambda)\cos\theta_{dh}$ and

$$L^{\uparrow}(\lambda,\theta_{out},\phi_{out};\theta_{dh},\phi_{dh}) = \frac{1}{\pi} R(\lambda,\theta_{out},\phi_{out},\theta_{dh},\phi_{dh}) E_0(\lambda)\cos\theta_{dh}\,. \qquad (4)$$

By inserting these expressions into Equations (1) or (3) we obtain the spectral directional-hemispherical (or “black-sky”) albedo $a^{dh}(\lambda;\theta_{dh},\phi_{dh})$:

$$a^{dh}(\lambda;\theta_{dh},\phi_{dh}) = \frac{1}{\pi}\int_{2\pi} R(\lambda,\theta_{out},\phi_{out},\theta_{dh},\phi_{dh})\cos\theta_{out} d\Omega_{out}\ . \qquad (5)$$

On the other hand, for completely diffuse illumination the down-welling radiance $L^{\downarrow}(\lambda,\theta_{in},\phi_{in}) = L_0(\lambda)$ is constant and the irradiance becomes $E^{\downarrow}(\lambda) = \pi L_0(\lambda)$. By

inserting these terms into Equation (3) and after making use of Equation (5) the spectral bi-hemispherical (or "white-sky") albedo $a^{bh}(\lambda)$ can be written as:

$$a^{bh}(\lambda) = \frac{1}{\pi} \int_{2\pi} a^{dh}(\lambda; \theta_{in}, \phi_{in}) \cos\theta_{in} d\Omega_{in} \ . \tag{6}$$

These two quantities, i.e. the functional dependencies $a^{dh}(\lambda; \theta_{dh}, \phi_{dh})$ and $a^{bh}(\lambda)$, are true surface properties and correspond to the limiting cases of point source $[a^{dh}(\lambda; \theta_{dh}, \phi_{dh})]$ and completely diffuse illumination $[a^{bh}(\lambda)]$. For partially diffuse illumination the actually occurring spectral albedo value may be approximated as a linear combination of the limiting cases

$$a(\lambda) = [1 - f_{diffuse}(\lambda)] a^{dh}(\lambda; \theta_s, \phi_s) + f_{diffuse}(\lambda)\, a^{bh}(\lambda) \,, \tag{7}$$

where $f_{diffuse}$ denotes the fraction of diffuse radiation and (θ_s, ϕ_s) the solar direction.

For many applications the quantity of interest is not the spectral but rather the broad-band albedo which is defined as the ratio of up-welling to down-welling radiation fluxes in a given wavelength interval $[\lambda_1, \lambda_2]$:

$$a_{[\lambda_1,\lambda_2]} := \frac{F^{\uparrow}_{[\lambda_1,\lambda_2]}}{F^{\downarrow}_{[\lambda_1,\lambda_2]}} = \frac{\int_{\lambda_1}^{\lambda_2} \int_{2\pi} L^{\uparrow}(\lambda, \theta_{out}, \phi_{out}) \cos\theta_{out} \ d\Omega_{out} d\lambda}{\int_{\lambda_2}^{\lambda_2} \int_{2\pi} L^{\downarrow}(\lambda, \theta_{in}, \phi_{in}) \cos\theta_{in} \ d\Omega_{in} d\lambda} \ . \tag{8}$$

In analogy to Equation (3) it can be expressed in terms of the bi-directional reflectance factor as

$$a(\lambda) = \frac{\frac{1}{\pi} \int_{\lambda_1}^{\lambda_2} \int_{2\pi} \int_{2\pi} R(\lambda, \theta_{out}, \phi_{out}, \theta_{in}, \phi_{in}) L^{\downarrow}(\lambda, \theta_{in}, \phi_{in}) \cos\theta_{in} \cos\theta_{out} \ d\Omega_{in} d\Omega_{out} d\lambda}{F^{\downarrow}_{[\lambda_1,\lambda_2]}} \ . \tag{9}$$

The directional-hemispherical broad-band albedo

$$a^{dh}_{[\lambda_1,\lambda_2]}(\theta_{dh}, \phi_{dh}) = \frac{\int_{\lambda_1}^{\lambda_2} a^{dh}(\lambda; \theta_{dh}, \phi_{dh}) E^{\downarrow}(\lambda) \, d\lambda}{\int_{\lambda_1}^{\lambda_2} E^{\downarrow}(\lambda) \, d\lambda} \tag{10}$$

and the bi-hemispherical broad-band albedo

$$a^{bh}_{[\lambda_1,\lambda_2]} = \frac{\int_{\lambda_1}^{\lambda_2} a^{bh}(\lambda) E^{\downarrow}(\lambda)\, d\lambda}{\int_{\lambda_1}^{\lambda_2} E^{\downarrow}(\lambda)\, d\lambda} \qquad (11)$$

can be written as integrals of the respective spectral quantities weighted by the spectral irradiance. In contrast to the spectral albedo quantities defined in Equations (5) and (6), the corresponding broad-band albedo values are not pure surface properties since the wavelength dependence of the spectral irradiance $E(\lambda)$ appearing as a weight factor in their definition may vary as a function of the atmospheric composition. In analogy to Equation (7) the broad-band albedo for partially diffuse illumination conditions may be expressed as a weighted average of $a^{dh}_{[\lambda_1,\lambda_2]}(\theta_s,\phi_s)$ and $a^{bh}_{[\lambda_1,\lambda_2]}$.

Satellite observations provide TOA-radiance measurements for certain configurations of the illumination and observation geometry. The calculation of surface albedo according to the equations above requires the knowledge of the complete bi-directional reflectance distribution function of the surface. To obtain an estimate of this quantity it is in principle necessary to solve the radiative transfer problem in the coupled surface-atmosphere system. In the LSA SAF system a simplified approach is adopted. In a first step an atmospheric correction is performed in order to derive TOC-reflectance values corresponding to the occurring angular observation configurations. In a second step a semi-empirical kernel-based reflectance model is adjusted to the measurements. This delivers an estimate of the complete angular dependence of the bi-directional reflectance factor R_β in the spectral channel β of the measuring instrument:

$$R_\beta(\theta_{out},\theta_{in},\phi) = \mathbf{k}_\beta \mathbf{f}\ (\theta_{out},\theta_{in},\phi)\ . \qquad (12)$$

Here $\mathbf{k}_\beta = (k_{0\beta}, k_{1\beta}, k_{2\beta}, ...)^{\mathrm{T}}$ and $\mathbf{f} = (f_0, f_1, f_2, ...)^{\mathrm{T}}$ represent vectors formed by the retrieved model parameters $k_{i\beta}$ and the kernel functions f_i, respectively. The individual azimuth angles were replaced by the relative azimuth angle ϕ between the directions of incoming and outgoing light paths. (This is possible without restriction of generality as long as the surface is considered as spatially isotropic.)

The algorithm consists in calculating the integrals (5) and (6) for determining albedo estimates a^{dh}_β and a^{bh}_β in all instrument channels β by applying the coefficients $\mathbf{k}_\beta$ provided by the directional reflectance model inversion. The narrow-band albedo values serve as an approximation to the spectral albedo at the central band wavelength λ_β. Furthermore broad-band albedo values a^{dh}_γ and a^{bh}_γ corresponding

to suitable intervals $\gamma = [\lambda_1, \lambda_2]$ are derived from the spectral estimates by employing appropriate approximations to the integrals (10) and (11).

2.3 Atmospheric Correction

The LSA SAF operational system provides TOA-radiances as well as all auxiliary information needed to perform the atmospheric correction at the temporal resolution of the image acquisition and the spatial resolution of the SEVIRI instrument. The required quantities include the illumination and observation angles, a land/water-mask, the cloud-mask product (CMa) generated with software components developed by the Nowcasting-SAF, surface pressure information obtained from the ECMWF numerical weather prediction model combined with the use of a digital elevation model, column water vapour from the ECMWF model, and ozone content estimated by using the TOMS climatology.

The measurements of the TOA-radiance $\hat{L}_\beta$ in the spectral channels of the SEVIRI instrument are first converted to TOA-reflectance factor values:

$$\hat{R}_\beta = \frac{\hat{L}_\beta}{B_\beta \, v(t) \cos\theta_s} \quad . \tag{13}$$

The "band factor" B_β depends on the solar spectral irradiance and the spectral sensitivity of the respective channel (Derrien, 2002). The numerical values currently used are 20.76 mW/(m^2 sr cm^{-1}), 23.24 mW/(m^2 sr cm^{-1}), and 19.85 mW/(m^2 sr cm^{-1}), respectively, for the 0.6µm, 0.8µm, and 1.6µm channels. The factor $v(t)$ takes into account the varying distance of the sun as a function of the day t of the year.

The atmospheric correction module is based on SMAC, a Simplified Method for the Atmospheric Correction of satellite measurements in the solar spectrum (Rahman and Dedieu, 1994). TOC-reflectance values R_β are calculated from the TOA-values $\hat{R}_\beta$ as

$$R_\beta = \frac{\tilde{R}_\beta}{1 + \tilde{R}_\beta S_\beta} \quad \text{with} \quad \tilde{R}_\beta = \frac{\hat{R}_\beta - T_\beta^{gas} R_\beta^{atm}}{T_\beta^{gas} T_\beta(\theta_s) T_\beta(\theta_v)} \tag{14}$$

where S_β is the spherical albedo of the atmosphere, T_β^{gas} is the total gaseous transmission, R_β^{atm} the "atmospheric reflectance", and $T_\beta(\theta_s)$ and $T_\beta(\theta_v)$ "atmospheric diffuse transmittances" as defined by Rahman and Dedieu (1994). These quantities, which characterise the atmospheric absorption and scattering processes, are calculated from information about the atmospheric constituents by means of parameterisations with simple analytic functions whose coefficients depend on the spectral response of the respective channel considered. For our application the relevant coefficients corresponding to the MSG 0.6µm, 0.8µm, and 1.6µm channels were provided by Berthelot (2001). A continental aerosol type is assumed

and the aerosol optical thickness at 550nm is currently specified according to a latitude dependent climatology (Berthelot et al.,1994) of the form

$$\tau_{aer} = 0.2\left[\cos(lat) - 0.25\right]\cos(lat)^3 + 0.05 \ , \qquad (15)$$

which is implemented in the operational system as a static file and can easily be replaced when a reliable real-time aerosol product becomes available in the future.

The TOC-reflectance values for the three used channels are determined for all SEVIRI scenes and are available as an internal product in the LSA SAF system. In the following methodological discussion we assume that all atmospheric effects are correctly accounted for and we consider the obtained results as true bi-directional reflectance factor values. In practice inaccurate knowledge of the atmospheric composition as well as simplifications in the correction approach can introduce random as well as systematic uncertainties.

2.4 Model Inversion

The observations provide a set of n reflectance measurements $R_{j\beta}$ $(j = 1, \cdots, n)$ in different spectral channels β given at irregularly spaced time points t_j and varying discrete values of the view θ_{vj} and solar zenith angles θ_{sj} (see Figure 3 for an example case). In the algorithm a linear kernel-based directional reflectance model of the form shown in Equation (12) is applied separately for each spectral band. In the following the index β referring to the channel is omitted to simplify the notation.

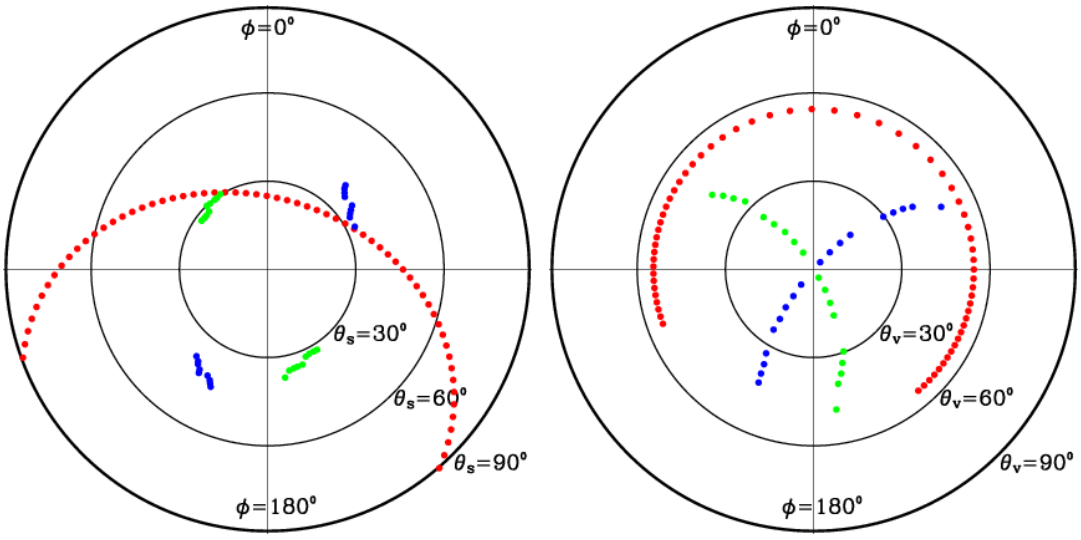


Figure 3: Illumination (left) and observation (right) geometries corresponding to a geographical location of [47° 47' N, 10° 37' E] and an observation period between the days of year 150 and 170. The relative azimuth angle ϕ is identical for the two graphs. The convention was chosen such that the top of the graphs (ϕ=0°)

corresponds to the backscattering regime. The colours of the dots denote observations taken by different sensors as follows: Red: SEVIRI/MSG, Green: AVHRR/METOP, Blue: AVHRR/NOAA.

The measurements provide a system of n linear equations

$$R_j(\theta_{vj},\theta_{sj},\phi_j)=\sum_{i=0}^{m-1} k_i\ f_i\ (\theta_{vj},\theta_{sj},\phi_j) \qquad (j=1,\cdots,n) \tag{16}$$

for constraining the m model parameters k_i $(i=0,\cdots,m-1)$. Introducing the vectors $\mathbf{k}=(k_0,k_1,...,k_{m-1})^{\mathrm{T}}$ and $\mathbf{R}=(R_1,R_2,...,R_n)^{\mathrm{T}}$, and the (n,m)-matrix $\mathbf{F}$ with the elements $F_{ji}=f_i\ (\theta_{vj},\theta_{sj},\phi_j)$, allows us to rewrite the equation system in matrix form:

$$\mathbf{R}=\mathbf{F}\mathbf{k}\,. \tag{17}$$

In general the number of available observations is larger than the number of parameters and no exact solution for $\mathbf{k}$ exists. However, the observed reflectances are affected by measurement errors and therefore it is convenient to search for the best solution in a statistical sense and to quantify the uncertainties of the retrieved parameter estimates. In this case it may turn out that a considerably larger number of observations than parameters are required in order to reasonably constrain the parameter values.

The uncertainties of the individual reflectance factor measurements R_j are quantified by means of weight factors w_j, which are related to the inverse of the standard "1-sigma" uncertainty estimates $\sigma[R_j]$. We introduce the scaled reflectance vector $\mathbf{b}$ with the elements $b_j=R_j w_j$ and the "design matrix" $\mathbf{A}$ with the elements $A_{ji}=F_{ji}w_j$ (see e.g. Press et al., 1995). The linear least squares solution to the inversion problem in Equation (17) can be found by solving the "normal equations"

$$(\mathbf{A}^{\mathrm{T}}\mathbf{A})\mathbf{k}=\mathbf{A}^{\mathrm{T}}\mathbf{b} \tag{18}$$

for the parameters $\mathbf{k}$. The uncertainty covariance matrix of the retrieved model parameters is given by

$$\mathbf{C}_{\mathbf{k}}=(\mathbf{A}^{\mathrm{T}}\mathbf{A})^{-1}\,. \tag{19}$$

The diagonal elements C_{jj} of this matrix represent the variance $\sigma^2[k_j]$ of the respective parameters k_j. The covariance between k_i and k_j is given by the off-diagonal elements C_{ij}.

If the matrix $\mathbf{A}^{\mathrm{T}}\mathbf{A}$ is "far from" singular, the solution can be found by simply multiplying Equation (18) "from the left" with $\mathbf{C_k} = (\mathbf{A}^{\mathrm{T}}\mathbf{A})^{-1}$. In most of the cases this is feasible with sufficient numerical accuracy. However, if a very small number of measurements are available and the angular configuration is unfavourable (which is more likely to occur for geo-stationary satellite observations) the application of robust techniques involving singular value decomposition (SVD) and/or QR-decomposition is necessary to limit the effects of numerical errors when calculating the parameter estimates $\mathbf{k} = (k_0, k_1, k_2)^{\mathrm{T}}$ and the uncertainty covariance matrix $\mathbf{C_k}$.

To improve the result of the parameter estimation it can be useful to add constraints on the parameters themselves in the inversion of the linear model (see e.g. Li et al., 2001; Hagolle et al. 2004; a related approach was also adopted by Pokrovsky et al. 2003). In the following we consider independent and uncorrelated a priori information on the parameters expressed in terms of the first and second moments (average and standard deviation, respectively) of their a priori probability distribution function, i.e. an estimate of the form

$$k_i = k_{i\,\mathrm{ap}} \pm \sigma_{\mathrm{ap}}[k_i] \ . \tag{20}$$

To simplify notation let us consider an example with m=3 and additional constraints for the two parameters k_1 and k_2. In this case adding the constraints of the form (20) to the equation system (16) corresponds to extending the (n, m)-matrix $\mathbf{A}$ to the (n+2, m)-matrix

$$\mathbf{A}^* = \begin{pmatrix} & \mathbf{A} & \\ 0 & \sigma_{\mathrm{ap}}^{-1}[k_1] & 0 \\ 0 & 0 & \sigma_{\mathrm{ap}}^{-1}[k_2] \end{pmatrix} \tag{21}$$

and to extending the vector $\mathbf{b}$ to $\mathbf{b}^* = (b_1, ..., b_n, k_{1\,\mathrm{ap}}\sigma_{\mathrm{ap}}^{-1}[k_1], k_{2\,\mathrm{ap}}\sigma_{\mathrm{ap}}^{-1}[k_2])^{\mathrm{T}}$. The linear least squares solution with a priori information is then obtained in the same way as above by solving the normal equations.

More generally, taking into account a multivariate Gaussian a priori probability distribution function for the parameters quantified by its first and second moments corresponds to re-writing Equations (18) and (19) in the form

$$(\mathbf{A}^{\mathrm{T}}\mathbf{A} + \mathbf{C}_{\mathrm{ap}}^{-1})\mathbf{k} = \mathbf{A}^{\mathrm{T}}\mathbf{b} + \mathbf{C}_{\mathrm{ap}}^{-1}\mathbf{k}_{\mathrm{ap}} \tag{22}$$

and

$$\mathbf{C_k} = (\mathbf{A}^{\mathrm{T}}\mathbf{A} + \mathbf{C}_{\mathrm{ap}}^{-1})^{-1} \tag{23}$$

with $\mathbf{k}_{\mathrm{ap}} = (k_{0\,\mathrm{ap}}, \ldots, k_{m-1\,\mathrm{ap}})^{\mathrm{T}}$ and the covariance matrix $\mathbf{C}_{\mathrm{ap}}$. For uncorrelated a priori information on the parameters the matrix $\mathbf{C}_{\mathrm{ap}} = \mathrm{diag}(\sigma_{\mathrm{ap}}^2[k_0], ..., \sigma_{\mathrm{ap}}^2[k_m])$ is diagonal.

Absence of a priori information on a given parameter – like it is the case for k_0 in the example case leading to the expression (21) – corresponds to $\sigma_{\mathrm{ap}}[k_i] \to \infty$ and $\sigma_{\mathrm{ap}}^{-2}[k_i] \to 0$.

By adding constraints on m-1 model parameters, the inversion can be carried out with a minimum number of one available observation. In addition, the constraints on the parameters reduce the condition number of the involved matrix and mitigate potential numerical problems. In practice we therefore add a regularisation term corresponding to $k_1 = 0.03 \pm 0.05$ and $k_2 = 0.3 \pm 0.5$ which does not lead to a noticeable prejudice in the inversion result.

2.5 Surface BRDF Model

In the following we restrict the discussion to a model with three parameters of the following form:

$$R(\theta_{out}, \theta_{in}, \phi) = k_0 + k_1 f_1(\theta_{out}, \theta_{in}, \phi) + k_2 f_2(\theta_{out}, \theta_{in}, \phi). \quad (24)$$

While k_0 quantifies an isotropic contribution to the reflectance factor ($f_0 = 1$), the functions f_1 and f_2, respectively, are often chosen to represent the angular distribution related to "geometric" and "volumetric" surface scattering processes. Roujean et al. (1992) suggest the following analytical expressions:

$$\begin{aligned} f_1(\theta_{out}, \theta_{in}, \phi) = {} & \frac{1}{2\pi}[(\pi - \phi)\cos\phi + \sin\phi]\tan\theta_{out}\tan\theta_{in} \\ & - \frac{1}{\pi}(\tan\theta_{out} + \tan\theta_{in} + \sqrt{\tan^2\theta_{out} + \tan^2\theta_{in} - 2\tan\theta_{out}\tan\theta_{in}\cos\phi}) \end{aligned} \quad (25)$$

(for $\phi \in [0, \pi]$) and

$$f_2(\theta_{out}, \theta_{in}, \phi) = \frac{4}{3\pi}\frac{1}{\cos\theta_{out} + \cos\theta_{in}}[(\frac{\pi}{2} - \xi)\cos\xi + \sin\xi] - \frac{1}{3} \quad (26)$$

with the phase angle

$$\xi = \arccos[\cos\theta_{out}\cos\theta_{in} + \sin\theta_{out}\sin\theta_{in}\cos\phi]. \quad (27)$$

Figure 4 depicts the dependence of these kernel functions on the zenith angle of the reflected light-ray for different illumination directions.

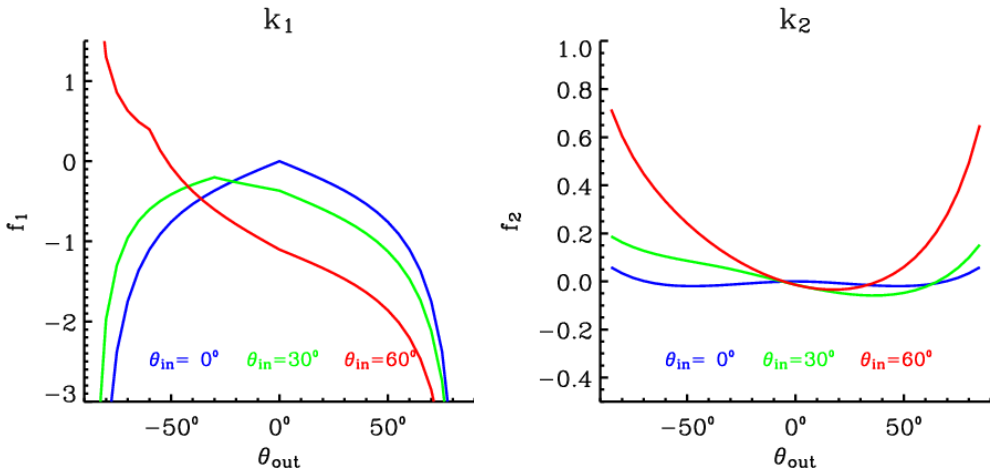


Figure 4: Angular dependence of the "geometric" (left) and "volume scattering" (right) kernels of the reflectance model introduced by Roujean et al. (1992). In the graphs negative zenith angle values correspond to the backscatter direction (relative azimuth angle ϕ=0°) and positive zenith angle values to the forward scatter direction (ϕ=180°).

2.6 Weighting of Measurements

Knowledge of the angular configurations for each measurement point t_j allows us to calculate the matrix $F_{ji} = f_i\ (\theta_{vj}, \theta_{sj}, \phi_j)$. In order to determine the scaled reflectance vector $\mathbf{b}$ and the design matrix $\mathbf{A}$ it is necessary to specify the weight factor w_j. We choose an expression of the form

$$w_j = w_\theta(\theta_{vj}, \theta_{sj}) w_t\ (t_j) \tag{28}$$

which simultaneously characterises the angular as well as the temporal dependence of the weight attributed to each measurement point.

In the present algorithm configuration the temporal weight function

$$w_t\ (t_j) = 1 \tag{29}$$

is kept constant since reflectance measurements for direct inversion are accumulated over a short composition period of one day only and the temporal composition of the daily observations is handled recursively as described in Section 2.8.

The angular component

$$w_\theta(\theta_{vj},\theta_{sj}) = \frac{1}{\sigma[R_j(\theta_{vj},\theta_{sj})]} \tag{30}$$

of the weight function is conveniently defined as the inverse of the estimated uncertainty of the reflectance measurements whose directional dependence is assumed to be a linear function of the relative air-mass $\eta(\theta_{vj},\theta_{sj})$:

$$\sigma[R_j(\theta_{vj},\theta_{sj})] = \sigma[R_j(\theta_v = 0°,\theta_s = 0°)]\,\eta(\theta_{vj},\theta_{sj})\,. \tag{31}$$

Estimates for the values of the reference uncertainties $\sigma[R_j(\theta_v = 0°,\theta_s = 0°)]$ at normalised geometry were obtained from a statistical analysis of atmospherically corrected SEVIRI scenes and are expressed as a linear function of the reflectance factor value

$$\sigma[R_j(\theta_v = 0°,\theta_s = 0°)] = c_1 + c_2 R_j \tag{32}$$

with coefficients for the three spectral bands as specified in Table 3. A lower limit of 0.005 and an upper limit of 0.05 are imposed for this quantity in order to avoid extreme values for reflectance outliers. A description of the method applied for obtaining the uncertainty estimates in a similar context is given in Geiger et al. (2005).

Table 3 Coefficients for the parameterisation of the TOC reflectance factor uncertainty estimates.

	0.6µm	0.8µm	1.6µm
c_1	0.001	0.005	0.000
c_2	0.07	0.02	0.04

For the inversion process all reflectance observations are taken into account for which the solar zenith angle as well as the view zenith angle do not exceed a threshold of 85°. In order to further decrease the weight for reflectance measurements taken at extreme angles close to this limit, the zenith angles are rescaled in the calculation of the relative air-mass in the following way:

$$\eta(\theta_{vj},\theta_{sj}) = \frac{1}{2}\left(\frac{1}{\cos\tilde{\theta}_{vj}} + \frac{1}{\cos\tilde{\theta}_{sj}}\right) \text{ with } \tilde{\theta}_{vj} = \theta_{vj}\frac{90°}{85°} \text{ and } \tilde{\theta}_{sj} = \theta_{sj}\frac{90°}{85°}\,. \tag{33}$$

The rationale of this prescription is potential systematic problems in the atmospheric correction for very large solar and view angles, for which the employed scheme was not specifically designed, as well as the divergence of the f_1 kernel function (cf. Figure 4).

In order to reduce the sensitivity to outliers due to undetected clouds, observations are eliminated from the analysis if the considered pixel is marked as cloudy in the

slot acquired directly before or afterwards. In addition, observations for which the respective flag of the cloud mask product CMa indicates a bad quality are penalised in the weighting scheme by multiplying the reflectance uncertainty estimate with a factor of 10. The same approach is adopted for the observations of pixels that might be contaminated by cloud shadow according to their location next to cloudy pixels and considering the solar azimuth direction. In this way the potentially affected observations are only significant in the inversion process if no "reliable" observations are available at all.

2.7 Illustration of the Model Inversion

In order to illustrate the functioning of the model inversion approach, Figure 5 depicts an example for the series of atmospherically corrected reflectance factor values obtained from the SEVIRI image slots acquired during one day as a function of the solar zenith angle. The bars attached to each data point (from the centre to each end) correspond to the uncertainty estimates used in the weighting scheme. Data points flagged as of bad quality in the cloud mask are marked in grey colour. Image slots for which the considered pixel was flagged as cloudy are marked with a rhombus symbol at the abscissa. In the shown example this occurs for a number of slots close to local solar noon at a zenith angle of roughly 26°. The solid lines in the graphs represent the result obtained by re-calculating the reflectance factor with Equation (17) from the retrieved best-fit model parameters in the same geometric configuration as the observations.

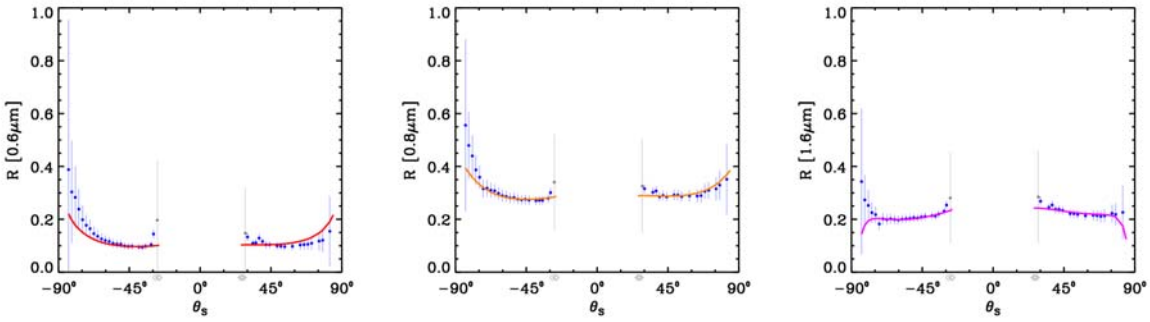


Figure 5: Example for the results of the TOC-reflectance model inversion in the three used SEVIRI channels (49.02°N, 2.53°E; 1st of July 2006). Negative values of the solar zenith angles correspond to observations acquired before local solar noon.

The interest of the model fit for albedo determination is to obtain an interpolation and extrapolation of the reflectance factor for geometric configurations that are not observed. For one of the spectral channels of the example case, Figure 6 depicts the modelled reflectance factor for different illumination directions. The graphs illustrate that the angular dependence becomes increasingly important for large incidence angles.

The top panels of the figure are for the principal plane and the bottom ones for the orthogonal plane which correspond, respectively, to vertical and horizontal sections of the polar graph shown on the right hand side of Figure 3. For the top panels negative values of the zenith angle θ_{out} correspond to the backscatter direction (ϕ=0°) and positive values to the forward scatter direction (ϕ=180°). The bottom panels, which are symmetric in θ_{out}, correspond to relative azimuth angles ϕ=90° and ϕ=270°.

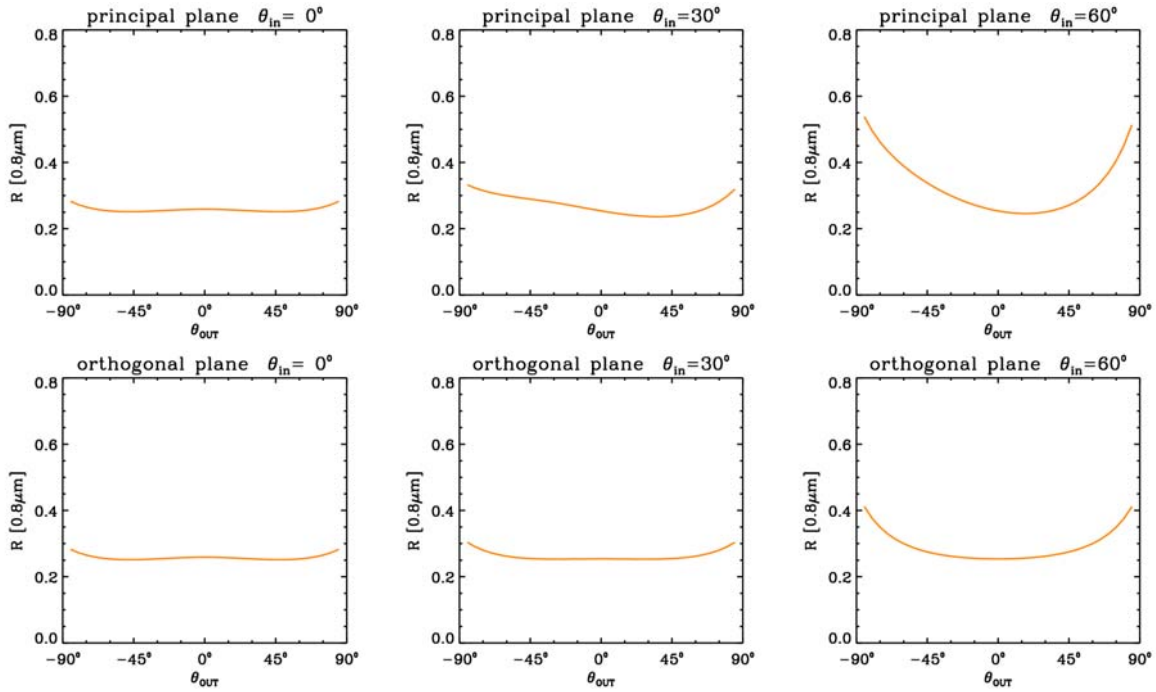


Figure 6: The dependence of the 0.8µm-channel reflectance factor on the direction of the outgoing light ray for different incidence directions according to the model fit of the example case from Figure 5.

2.8 Temporal Composition

In order to reduce the sensitivity of the resulting daily estimates to reflectance outliers and extended periods of missing data because of persistent cloudiness, it is necessary to combine the information over a longer time period. A recursive scheme is applied for this purpose. At each execution of the algorithm the previous parameter estimate $\mathbf{k}_{\text{in}}$ and the corresponding uncertainty measure $\mathbf{C}_{\mathbf{k}}^{\text{in}}$ is read from the relevant internal product files. Since these quantities now serve as input information, the index or exponent “in” was added to the symbols in order to distinguish them from the new estimates to be derived. The previous estimates are then used in the following way as a priori information for the linear model inversion specified in Equations (22) and (23):

$$\mathbf{k}_{\text{ap}} = \mathbf{k}_{\text{in}}$$
$$\mathbf{C}_{\text{ap}} = \mathbf{C}_{\mathbf{k}}^{\text{in}} \, (1+\Delta)^{(t_0 - t_{\text{in}})/\Delta t} \text{ (with } \Delta t = 1\text{day)}. \quad (34)$$

The multiplicative factor (larger than one) applied to the covariance matrix reduces the confidence in the a priori estimate as a function of the lapse of time $t_0 - t_{\text{in}}$ since the previous execution of the algorithm. The result of the inversion, constrained in this way with a priori information obtained from previous observations, is mathematically equivalent to performing the inversion directly with the complete set of observations by attributing less weight to those observations acquired before the day t_0. A multiplicative factor in the weights translates into the inverse of the square root of this factor in the elements of the covariance matrix resulting from the model inversion. The recursive multiplication process can therefore be identified with the presence of an effective temporal weight function [cf. Equation (28)] of the form

$$w_t(t) = (1+\Delta)^{-(t_0 - t)/(2\Delta t)} \text{ for } t \le t_0$$
$$w_t(t) = 0 \text{ for } t > t_0 \quad (35)$$

which is shown in Figure 7. The quantity Δ can be related to the characteristic temporal scale τ (full width at half mean) of this weight function. The latter was chosen as 5 days in the present configuration of the algorithm running in the operational system. This value represents a compromise between temporal resolution and sensitivity to remaining small scale variations in the reflectance factor values which are due to uncorrected atmospheric effects.

If no new observations are available during the whole day due to persistent cloudiness, the estimate for the model parameters $\mathbf{k}$ remains unchanged and only the multiplicative factor is applied for the covariance matrix as in Equation (34). The "age" of the last observation exploited in the recursive inversion scheme is an important piece of information for potential applications and is therefore also made available to the users.

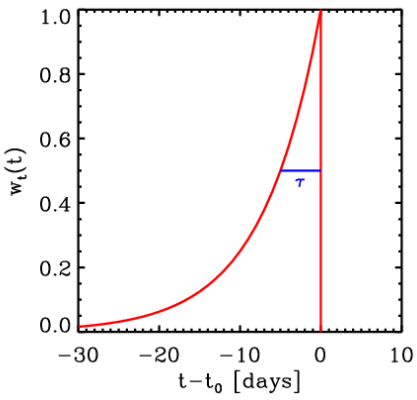


Figure 7: Effective temporal weight function in the recursive composition scheme. The characteristic time scale is τ = 5 days.

In line with the real-time strategy of LSA SAF the implemented method makes it possible to deliver the best estimate of the state of the land surface at the time of product generation and distribution by giving the largest weight to the most recent observations. At the same time owing to the successive accumulation of information a complete spatial coverage is achieved without the need for static surface information databases. Conceptually the implemented recursive composition scheme is similar to a Kalman-filter without intrinsic time evolution of the model (cf. Samain, 2005).

2.9 Angular Integration

Inserting the reflectance model (12) in the albedo definitions (5) and (6) gives the expressions

$$a_\beta^{dh}(\theta_{in}) = \mathbf{k}_\beta \mathbf{I}^{dh}(\theta_{in}) \quad \text{and} \quad a_\beta^{bh} = \mathbf{k}_\beta \mathbf{I}^{bh} \tag{36}$$

for the spectral albedo quantities, where

$$I_i^{dh}(\theta_{in}) = \frac{1}{\pi}\int_0^{2\pi}\int_0^{\pi/2} f_i\,(\theta_{out},\theta_{in},\phi)\cos(\theta_{out})\sin(\theta_{in})d\theta_{out}d\phi$$
$$\text{and} \quad I_i^{bh} = 2\int_0^{\pi/2} I_i^{dh}(\theta_{in})\cos(\theta_{in})\sin(\theta_{in})d\theta_{in} \tag{37}$$

are the respective angular integrals of the fixed kernel functions which can conveniently be pre-computed and stored in look-up tables. Figure 8 shows the illumination angle dependence of the directional-hemispherical integrals of the three kernels according to the model introduced by Roujean et al. (1992), which is currently used in the operational system.

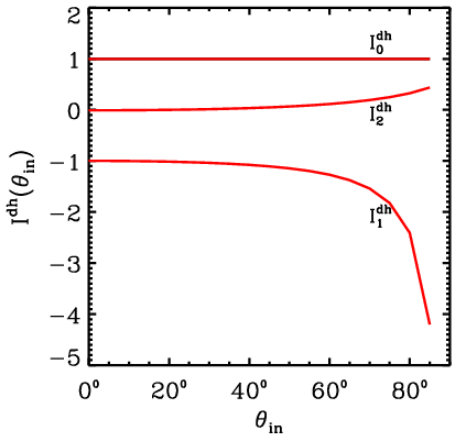


Figure 8: Illumination zenith angle dependence of the directional-hemispherical kernel integrals for the Roujean et al. (1992) model.

Thanks to the linear relationship [Equation (36)] between the BRDF-model parameters and each of the spectral albedo quantities, standard uncertainty estimates for the latter can conveniently be derived from the respective uncertainty covariance matrix $\mathbf{C_k}$ of the model parameters (cf. Lucht and Lewis, 2000) and the appropriate kernel integrals $\mathbf{I}$:

$$\sigma[a] = \sqrt{\mathbf{I}^{\mathrm{T}}\mathbf{C_k}\mathbf{I}} \quad . \tag{38}$$

Figure 9 shows the dependence of the directional-hemispherical albedo on the illumination zenith angle according to the result of the model fit for the example case discussed in Section 2.7. In the graphs an increase of a^{dh} with rising θ_{in} can be noticed which is characteristic for most types of land surfaces.

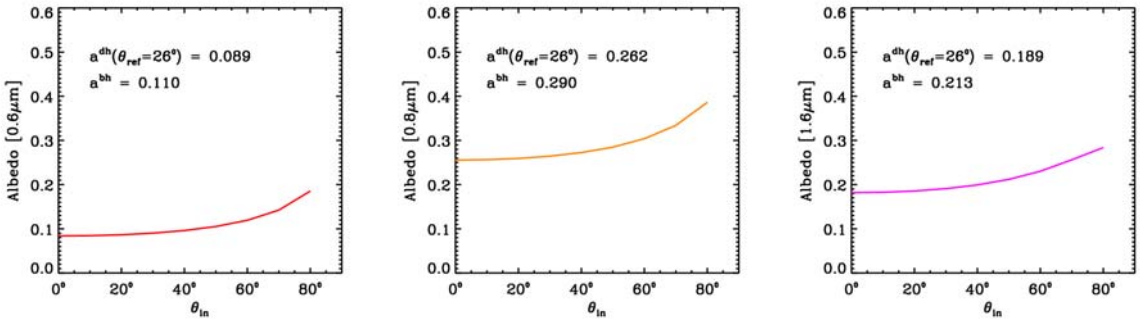


Figure 9: Dependence of the directional-hemispherical albedo on the illumination zenith angle for the example case from Figure 5. The value at the reference angle θ_{ref} and the bi-hemispherical estimate are indicated.

In the LSA SAF albedo product files the directional-hemispherical albedo $a^{dh}(\theta_{ref})$ for a specific reference angle θ_{ref} as well as the bi-hemispherical albedo a^{bh} are delivered. The solar position at local noon was chosen as the directional reference for the former, which means that the zenith angle θ_{ref} is determined as a function of each pixel's geographic coordinates and the day of the year. For the time being the information on the complete functional dependence $a^{dh}(\theta_{in})$ is not available in the (external) product files. Appropriate empirical formulae (e.g. Dickinson 1983, Briegleb et al. 1986) may be applied for modelling the evolution of directional-hemispherical albedo $a^{dh}(\theta_s)$ according to the daily solar cycle. Finally, Equation (7) can be applied to calculate a weighted average of the directional and bi-hemispherical estimates as a function of the fraction of diffuse radiation in order to approximate a real sky situation.

As it can be seen from Figure 8, the directional-hemispherical integral $I_1^{dh}(\theta_{in})$ of the used kernel function f_1 tends to diverge as the illumination zenith angle approaches 90°. This may lead to a potential problem for the directional-hemispherical albedo when the illumination zenith angle is very large. However, the numerical values of the parameter k_1 are usually one order of magnitude smaller than k_2, which mitigates the apparent dominance of the f_1 kernel in the angular dependence of the integrals $I_i^{dh}(\theta_{in})$. In the algorithm an upper limit of 85° is specified for the reference angle θ_{ref} in the calculation of the directional-hemispherical albedo variant. Also, under such conditions the fraction of diffuse radiation becomes dominant, and the directional-hemispherical albedo is then of little relevance for practical purposes. Owing to the weighting with the cosine of the illumination angle in the bi-hemispherical integral of Equation (37), the divergence of $I_1^{dh}(\theta_{in})$ is unproblematic for the bi-hemispherical albedo variant.

2.10 Narrow- to Broad-band Conversion

The kernel approach offers a description of the angular dependence of the reflectance factor. It is applied to each instrument channel separately and provides no information on the spectral behaviour outside of the available narrow bands. Broad-band albedo is defined as the integral of spectral albedo over a certain wavelength interval weighted by the spectral irradiance [Equations (10) and (11)]. Since the integral can be approximated as a weighted sum of the integrand at discrete values of the integration variable, broad-band albedo may be expressed as a linear combination of the spectral (or rather narrow-band) albedo values in the available instrument channels.

In the LSA SAF algorithm the broad-band albedo estimates for a given target interval γ are derived from the spectral quantities by applying a linear transformation of the form

$$a_\gamma = c_{0\gamma} + \sum_\beta c_{\beta\gamma} a_\beta \qquad (39)$$

with coefficients $c_{0\gamma}$ and $c_{\beta\gamma}$ as summarised in Table 4. Three different broad-band albedo intervals are considered: the total short-wave range from 0.3µm to 4µm, the visible wavelength range from 0.4µm to 0.7µm, as well as the near infrared range from 0.7µm to 4µm.

The narrow- to broad-band conversion coefficients were determined by van Leeuwen and Roujean (2002). Those authors performed a linear regression analysis based on radiative transfer simulations. They generated an extensive data set of synthetic spectral canopy reflectances for different surface types by using the ASTER spectral library (Hook, 1998) and the SAIL radiative transfer model (Verhoef, 1984). After calculating the narrow-band albedo values in the SEVIRI instrument's spectral bands

and the broad-band albedo values in the ranges of interest, they then determined the corresponding linear transformation coefficients.

Table 4 Narrow- to broad-band conversion coefficients for the SEVIRI channels (van Leeuwen and Roujean, 2002).

γ	$c_{0\gamma}$	$c_{1\gamma}$ (0.6µm)	$c_{2\gamma}$ (0.8µm)	$c_{3\gamma}$ (1.6µm)
[0.3µm, 4µm]	0.004724	0.5370	0.2805	0.1297
[0.4µm, 0.7µm]	0.009283	0.9606	0.0497	-0.1245
[0.7µm, 4µm]	-0.000426	0.1170	0.5100	0.3971

The spectral properties of snow are rather different from those of ordinary land surfaces and the narrow- to broad-band conversion cannot be well described with the same linear relation. For pixels flagged as snow-covered in the CMa cloud mask product we therefore use the different set of coefficients listed in Table 5, which were determined with a similar regression analysis as described above.

Table 5 Narrow- to broad-band conversion coefficients for pixels flagged as snow-covered calculated with tools developed by Samain (2005).

γ	$c_{0\gamma}$	$c_{1\gamma}$ (0.6µm)	$c_{2\gamma}$ (0.8µm)	$c_{3\gamma}$ (1.6µm)
[0.3µm, 4µm]	0.0175	0.3890	0.3989	-0.0141
[0.4µm, 0.7µm]	0.0155	0.7536	0.2596	-0.5349
[0.7µm, 4µm]	0.0189	0.0942	0.5090	0.4413

The weighting with the spectral irradiance in the definition of the broad-band albedo introduces a dependence on the atmospheric conditions since the spectral properties of the incident solar radiation are different in clear and overcast sky situations. However for the time being this difference has not been taken into account in the generation of the input data sets for the regression analysis and the same narrow- to broad-band conversion relations are applied for the directional-hemispherical albedo $a^{dh}(\theta_{ref})$, irrespective of the reference illumination angle, and for the bi-hemispherical albedo variant.

Assuming that the errors of the spectral albedo estimates are uncorrelated, the uncertainty estimate for the broad-band albedo quantities is given by

$$\sigma[a_\gamma] = \sqrt{\sigma^2_{\text{Regression}} + \sum_\beta (c_{\beta\gamma})^2 \sigma^2[a_\beta]} \qquad (40)$$

where $\sigma^2_{\text{Regression}} = 0.01$ denotes the estimated residual variance of the linear regression.

2.11 Signification of the Uncertainty Estimates

The (theoretical) uncertainty estimates for the respective albedo quantities represent the most general quality indicator operationally delivered by the algorithm. They are calculated for each pixel as a function of the respective observation conditions. The validity of these estimates is strictly speaking restricted to the framework of the applied BRDF-model and their quantitative pertinence needs to be checked with appropriate validation studies.

Determining the best solution of the linear model inversion problem in a least square sense implicitly includes the assumption that the probability distributions of the errors of the TOC-reflectance factor values are Gaussian and mutually uncorrelated, i.e. their uncertainty covariance matrix $\mathbf{C_R} = \mathrm{diag}(\sigma^2[R_1],...,\sigma^2[R_n])$ is diagonal. In practice correlated errors may occur owing to instrument calibration uncertainties and systematic biases in the applied atmospheric correction scheme (or in the estimates of the concentration of atmospheric constituents used as input quantities for the correction). The uncertainty covariance matrix obtained for the model parameters therefore also only quantifies the uncertainties due to the non-correlated (random) part of the input observation error structure.

When a large number of observations are available during clear periods the respective uncertainties for the model parameters become formally very small, which indicates that the model is then very well constrained. The albedo is calculated from the model parameters by linear expressions and the albedo uncertainty estimates are obtained by propagating those of the model parameters. Hence the albedo uncertainty estimates preserve the formal Gaussianity and they also reflect uncertainties due to the non-correlated part of the reflectance error structure while correlated (systematic) errors are not taken into account. The instrument calibration uncertainty may be taken into account a posteriori in a simplified way by “root-sum-squared-addition” to the delivered albedo uncertainty estimates.

With the implementation of the recursive temporal composition method, the uncertainty estimates also express the temporal aspect of the relevance of the observations. In periods without useful observations the uncertainty increases. This reflects the decreasing confidence in the parameter estimate due to “ageing” of the information on which the estimate is based.

Non-Gaussian outliers in the reflectance observations owing to undetected clouds cause another potential problem for the uncertainty treatment. Imperfections in the cloud screening method can lead to a significant contribution of outliers in the probability density distributions of the top-of-canopy reflectance errors. This can affect the quality of the inversion results as well as the validity of the uncertainty estimates. Nevertheless, the strategies employed for penalising or eliminating potentially unreliable observations reduce the importance of this problem.

3 Product Description

3.1 Overview

In the LSA SAF operational system the four geographical regions depicted in Figure 1 are processed separately. The main characteristics of these windows are listed in Table 6. The projection and spatial resolution correspond to the characteristics of the Level 1.5 MSG/SEVIRI instrument data. Information on geo-location and data distribution are available on the LSA SAF website: http://landsaf.meteo.pt. The albedo product is calculated on a daily basis. Typically the algorithm is launched a little after midnight (UTC) and exploits MSG input data accumulated during the past day.

Table 6 Characteristics of the four LSA SAF geographical areas: Each region is defined by the corner positions relative to an MSG image of 3712 columns per 3712 lines with indices starting at 1 in the North and West.

Region Name	Description	Initial Column	Final Column	Initial Line	Final Line	Size in Columns	Size in Lines	Total Number of Pixels
Euro	Europe	1550	3250	50	700	1701	651	1.107.351
Nafr	Northern Africa	1240	3450	700	1850	2211	1151	2.544.861
Safr	Southern Africa	2140	3350	1850	3040	1211	1191	1.442.301
SAme	Southern America	40	740	1460	2970	701	1511	1.059.211

3.2 Geolocation / Rectification

The DSSF SEVIRI-based (MDSSF) fields are generated pixel-by-pixel, maintaining the original resolution of SEVIRI level 1.5 data. These correspond to rectified images to 0º longitude, which present a typical geo-reference uncertainty of about 1/3 of a pixel. Data are kept in the native geostationary projection.
Files containing the latitude and longitude of the centre of each pixel may be downloaded from the Land-SAF website (http://landsaf.meteo.pt; under “Static Data and Tools”):

Longitude
HDF5_LSASAF_MSG_LON_Euro_200512201600.bz2

HDF5_LSASAF_MSG_LON_NAfr_200505191503.bz2
HDF5_LSASAF_MSG_LON_SAfr_200505191525.bz2
HDF5_LSASAF_MSG_LON_SAme_200505191527.bz2

Latitude

HDF5_LSASAF_MSG_LAT_Euro_200512201600.bz2
HDF5_LSASAF_MSG_LAT_NAfr_200505191503.bz2
HDF5_LSASAF_MSG_LAT_SAfr_200505191525.bz2
HDF5_LSASAF_MSG_LAT_SAme_200505191527.bz2

Alternatively, since the data are in the native geostationary projection, centred at 0º longitude and with a sampling distance of 3 km at the sub-satellite point, the latitude and longitude of any pixel may be easily estimated. Given the pixel column number, *ncol* (where *ncol*=1 correspond to the westernmost column of the file), and line number, *nlin* (where *nlin*=1 correspond to the northernmost line), the coordinates of the pixel may be estimated as follows:

$$lon = arctg\left(\frac{s_2}{s_1}\right) + sub_lon$$ longitude (deg) of pixel centre

$$lat = arctg\left(p_2 \cdot \frac{s_3}{s_{xy}}\right);$$ latitude (deg) of pixel centre

where

sub_lon is the sub-satellite point ($sub_lon = 0$)

and

$$s_1 = p_1 - s_n \cdot \cos x \cdot \cos y$$
$$s_2 = s_n \cdot \sin x \cdot \cos y$$
$$s_3 = -s_n \cdot \sin y$$
$$s_{xy} = \sqrt{s_1^2 + s_2^2}$$
$$s_d = \sqrt{(p_1 \cdot \cos x \cdot \cos y)^2 - (\cos^2 y + p_2 \cdot \sin^2 y) \cdot p_3}$$
$$s_n = \frac{p_1 \cdot \cos x \cdot \cos y - s_d}{\cos^2 y + p_2 \cdot \sin^2 y}$$

where

$$x = \frac{ncol - COFF}{2^{-16} \cdot CFAC}$$ (in Degrees)

$$y = \frac{nlin - LOFF}{2^{-16} \cdot LFAC}$$ (in Degrees)

$p_1 = 42164$
$p_2 = 1.006803$
$p_3 = 1737121856$

$CFAC$ =13642337

LFAC=13642337

The CFAC and LFAC coefficients are column and line scaling factors, which depend on the specific segmentation approach of the input SEVIRI data. Finally, COFF and LOFF are coefficients depending on the location of the each Land-SAF geographical area within the Meteosat disk. These are included in the file metadata (HDF5 attributes; Annex B), and correspond to one set of the values detailed below per SEVIRI/MSG area:

Table 7 Maximum values for number of columns (ncol) and lines (nlin), for each Land-SAF geographical area, and the respective COFF and LOFF coefficients needed to geo-locate the data.

Region Name	Description	Maximum *ncol*	Maximum *nlin*	COFF	LOFF
Euro	Europe	1701	651	308	1808
NAfr	Northern Africa	2211	1151	618	1158
SAfr	Southern Africa	1211	1191	-282	8
SAme	Southern America	701	1511	1818	398

3.3 File Formats

At each execution the albedo algorithm generates two types of (external) output files: Broad-band albedo estimates are included in a single file with the name convention

HDF5_LSASAF_MSG_ALBEDO_Region_YYYYMMDD0000

where **Region**, **YYYY**, **MM**, and **DD**, respectively, denote the region name, year, month, and day of data acquisition. For each of the three channels used by the algorithm the spectral albedo estimates are delivered in separate files respecting the name convention

HDF5_LSASAF_MSG_AL-C?-D!!_Region_YYYYMMDD0000

where **?=1,2,3** denotes the 0.6µm, 0.8µm, and 1.6µm channels, respectively, and where **!!=01 or 30** denotes the number of days for synthesis. For distribution via EumetCast the prefix ”S-LSA_-“ is added.

The LSA SAF products are provided in the HDF5 format developed by the NCSA (National Center for Supercomputing Applications) at the University of Illinois. A

comprehensive description as well as libraries for handling HDF5-files in Fortran and C are available at http://hdf.ncsa.uiuc.edu/HDF5.
A user friendly graphical interface to open and view HDF5-files can be downloaded from http://hdf.ncsa.uiuc.edu/hdf-java-html/hdfview/. The HDF5-format permits the definition of a set of attributes for providing relevant information. Each LSA SAF product file includes the general attributes listed in Table 11 of Appendix C. Within the HDF5-files the information is organised in the form of separate datasets. For each dataset a set of additional attributes is available (Table 12 of Appendix C).

3.4 Product Content

The broad-band albedo product file contains ten datasets comprising four albedo quantities, their respective uncertainty estimates, the quality flag, and the "age" of the information. Table 8 shows the list of quantities in the corresponding order of the datasets in the HDF5 structure. Directional-hemispherical values are calculated for each of the intervals γ: total short-wave (BB): [0.3µm, 4µm], near infrared (NI): [0.7µm, 4µm], and visible (VI): [0.4µm, 0.7µm]. Bi-hemispherical estimates are only available for the total short-wave range. As an example Figure 10 shows images for one of the albedo quantities, its respective uncertainty estimate, the quality flag, and the age of the information.

Table 8 Content of the broad-band surface albedo product files.

Parameter	Dataset Name	Unit	Range	Variable Type	Scale Factor
$a^{bh}_{[0.3\mu m,\,4\mu m]}$	AL-BB-BH	1	[0, 1]	2-Byte Signed Integer	10000
$\sigma[a^{bh}_{[0.3\mu m,\,4\mu m]}]$	AL-BB-BH-ERR	1	[0, 1]	2-Byte Signed Integer	10000
$a^{dh}_{[0.3\mu m,\,4\mu m]}$	AL-BB-DH	1	[0, 1]	2-Byte Signed Integer	10000
$\sigma[a^{dh}_{[0.3\mu m,\,4\mu m]}]$	AL-BB-DH-ERR	1	[0, 1]	2-Byte Signed Integer	10000
$a^{dh}_{[0.7\mu m,\,4\mu m]}$	AL-NI-DH	1	[0, 1]	2-Byte Signed Integer	10000
$\sigma[a^{dh}_{[0.7\mu m,\,4\mu m]}]$	AL-NI-DH-ERR	1	[0, 1]	2-Byte Signed Integer	10000
$a^{dh}_{[0.4\mu m,\,0.7\mu m]}$	AL-VI-DH	1	[0, 1]	2-Byte Signed Integer	10000
$\sigma[a^{dh}_{[0.4\mu m,\,0.7\mu m]}]$	AL-VI-DH-ERR	1	[0, 1]	2-Byte Signed Integer	10000
Quality Flag	Q-Flag	na	[0, 255]	1-Byte Unsigned Integer	na
Age of Information[1]	Z_Age	days	[0, 127]	1-Byte Signed Integer	1

[1] Note that this attribute is not present for the D30 product.

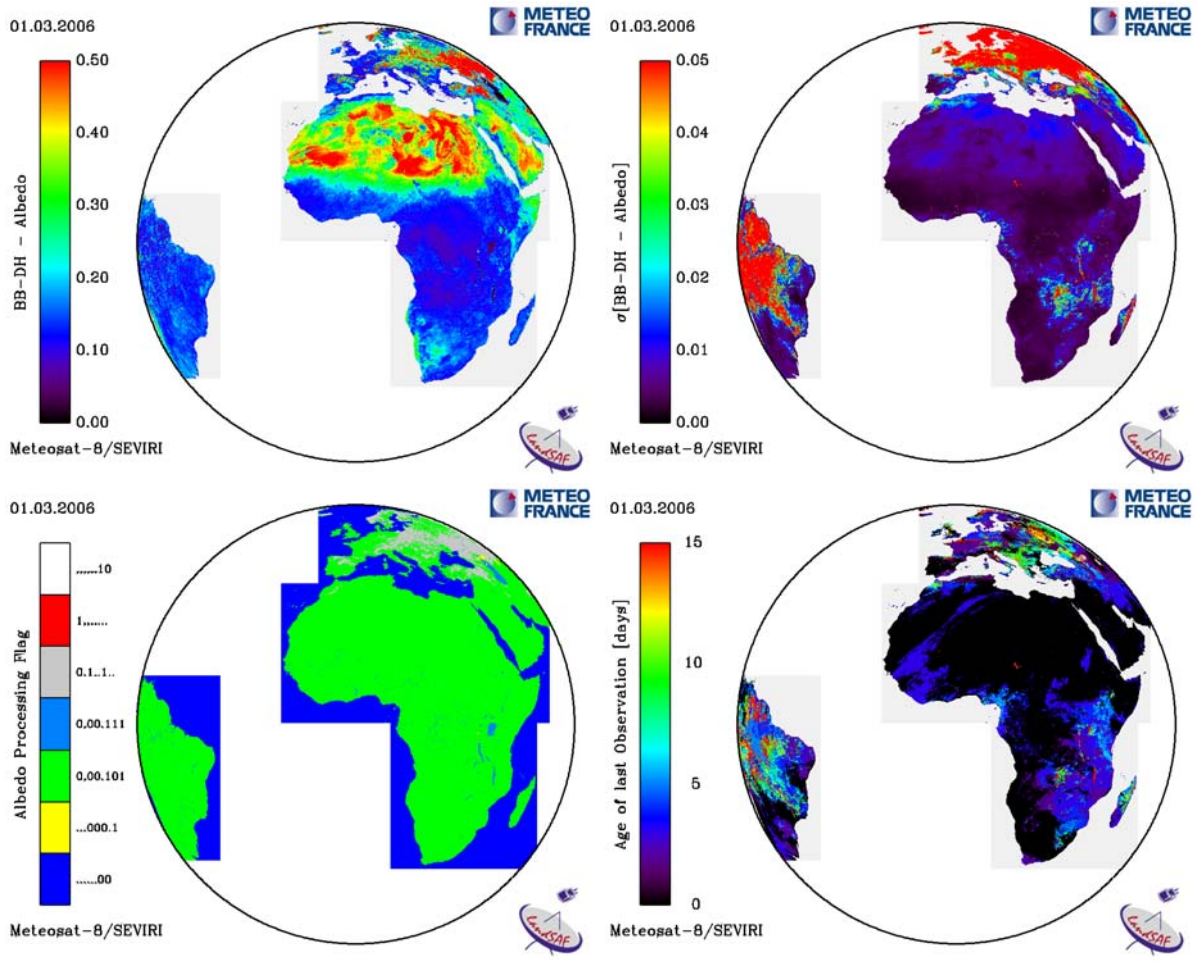


Figure 10: Broad-band albedo product for the 1st of March 2006. The top left panel shows the total broad-band directional-hemispherical albedo, the top right panel the corresponding uncertainty estimate, and the bottom left panel the quality flag. For the latter the legend indicates which bits were used for the visualisation, e.g. "……00" signifies that pixels with bits 0 and 1 equal to zero are depicted in dark blue colour. The bottom right panel shows the "age" of the last available observation used for each image pixel.

Each of the spectral albedo files contains four datasets comprising two albedo quantities, their respective uncertainty estimates, the quality flag and the age of the information. The technical details are given in Table . For illustration a colour composite, derived by combining the spectral albedo estimates from the three spectral output files, is shown in Figure 11.

Table 9 Content of the spectral surface albedo product files for each channel β.

Parameter	Dataset Name	Unit	Range	Variable Type	Scale Factor
a_β^{bh}	AL-SP-BH	1	[0, 1]	2-Byte Signed Integer	10000
$\sigma[a_\beta^{bh}]$	AL-SP-BH-ERR	1	[0, 1]	2-Byte Signed Integer	10000
a_β^{dh}	AL-SP-DH	1	[0, 1]	2-Byte Signed Integer	10000
$\sigma[a_\beta^{dh}]$	AL-SP-DH-ERR	1	[0, 1]	2-Byte Signed Integer	10000
Quality Flag	Q-Flag	na	[0, 255]	1-Byte Unsigned Int.	na
Age of Information	Z_Age	days	[0, 127]	1-Byte Signed Integer	1

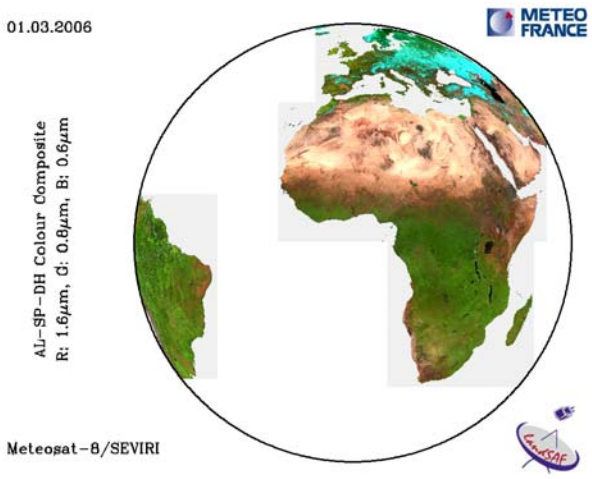


Figure 11: Colour composite derived from the three spectral directional-hemispherical albedo estimates for the 1st of March 2006.

Finally, Table 10 lists the signification of the numerical values of the (spectral and broad-band) albedo quality flag. Bits 0 and 1 propagate the land/sea mask information. Bits 2 to 4 indicate if MSG observations, EPS information, or additional external information, respectively, were used to produce the result. (The latter two bits are never set in the presently available product files, since up to now only MSG data have been processed.) Bit 5 indicates whether a pixel was flagged as snow covered in the NWC-CMa product for at least one slot of the daily time series.

(Note that the "Age of Information" dataset is available in the broad-band and spectral albedo product files since version 6.0 implemented in September 2006. The respective graph for an earlier date shown in Figure 10 was generated from internal product files in which this information was already available before.)

Table 10 Albedo product quality flag information.

Bit		Binary Code	Description
Bits 0-1	Land Sea Mask	00	Ocean
		01	Land
		10	Space (Outside of MSG disk)
		11	Continental water
Bit 2	MSG	0	No MSG Observations
		1	Including MSG Observations
Bit 3	EPS	0	No EPS Observations
		1	Including EPS Observations
Bit 4	External Information	0	No External Information
		1	Including External Information
Bit 5	Snow	0	No Snow
		1	Snow
Bit 6	Unused	0	-
		1	-
Bit 7	Failure	0	Normally Processed
		1	Algorithm Failed

3.5 Summary of Product Characteristics

Product Name: Land Surface Albedo

Product Code: AL

Product Level: Level 3

Product Parameters:

Coverage: MSG full disk (Continental pixels)

Packaging: Europe, N_Africa, S_Africa, S_America

Sampling: pixel by pixel basis

Spatial Resolution: MSG/SEVIRI full resolution (3km×3km at nadir)

Projection: MSG/SEVIRI Level 1.5 data projection

Units: dimensionless

Range: 0 - 1

Accuracy: objective: 10%; (to be confirmed)

Format:	16 bits signed integer (albedo and uncertainty estimates) 8 bits (quality flag and age of information)
Frequency of Generation:	daily
Size of Product Files:	Broad-band Albedo: 6Mb - 16Mb Spectral Albedo: 4Mb – 9Mb for each channel (depending on the continental window and the compression efficiency)

Additional Information:

Identification of bands used in algorithm:

MSG VIS 0.6

MSG NIR 0.8

MSG SWIR 1.6

Assumptions on SEVIRI input data:

Radiometric and Geometric Calibration

Identification of ancillary and auxiliary data:

Land/Sea Mask
Cloud Mask (CMa from NWC SAF software)
View Azimuth and Zenith Angles (from LSA SAF System)
Solar Azimuth and Zenith Angles (from LSA SAF System)
Pixel Latitude (from LSA SAF System)
Total Column Water Vapour (from ECMWF model)
Ozone Content (based on TOMS climatology)
Atmospheric Pressure (from ECMWF model)
Aerosol Optical Thickness at 550 nm (based on a climatology)
Digital Elevation Model (based on USGS GTOPO30)

4 Validation

As specified in the User Requirements Document the objective for the relative accuracy of the total short-wave broad-band albedo product is 10% (with reference to the respective albedo level). In this chapter the results of a comparison study with the MODIS albedo product are summarised and some known problems and limitations are mentioned. A more extended description of the results of the validation studies will be included in subsequent versions of the Product User Manual.

4.1 Comparison with the MODIS Albedo Product

The broad-band albedo product has been (indirectly) validated within the European continental window by comparing it to the respective product derived from observations of the MODIS instrument, which is generally considered as being of good quality and suitable as a reference quantity. The higher resolution MODIS product was re-projected to the MSG/SEVIRI grid. For each original MODIS pixel the "closest" SEVIRI pixel was determined and afterwards the albedo estimates for all MODIS pixels assigned to a given SEVIRI pixel were averaged. The MODIS product is generated with a temporal composition window of 16 days. In order to reproduce the temporal characteristics as closely as possible with the MSG data, the internal TOC-reflectance files provided by the operational system were re-processed to generate daily albedo estimates, which were then averaged over the relevant MODIS period. For expressing the validation results in a quantitative way the bias - defined as the average of the difference between the two estimates - and the standard deviation of that difference are considered. The temporal evolution of the validation statistics from June 2005 to September 2006 is visualised in Figure 12. The calculation of the statistics was restricted to those pixels for which the Land-SAF uncertainty estimate is below 0.10 and the MODIS quality flag indicates a high confidence.

During most of the period except winter the biases between the LSA SAF and MODIS products are negligible for the near infrared and total short-wave ranges and in the order of +0.015 for the visible broad-band range. The standard deviation in absolute units ranges between 0.015 for the visible and up to 0.03 for the near-infrared and total short-wave ranges. However, owing to the lower level of the albedo values, the discrepancies in relative units are the largest for the visible broad-band estimates. In winter the results tend to deteriorate, which is probably related to the unfavourable observation conditions (clouds, low solar elevation), the much smaller number of data points entering the validation statistics, and the different treatment of snow cover in the LSA SAF and MODIS algorithms.

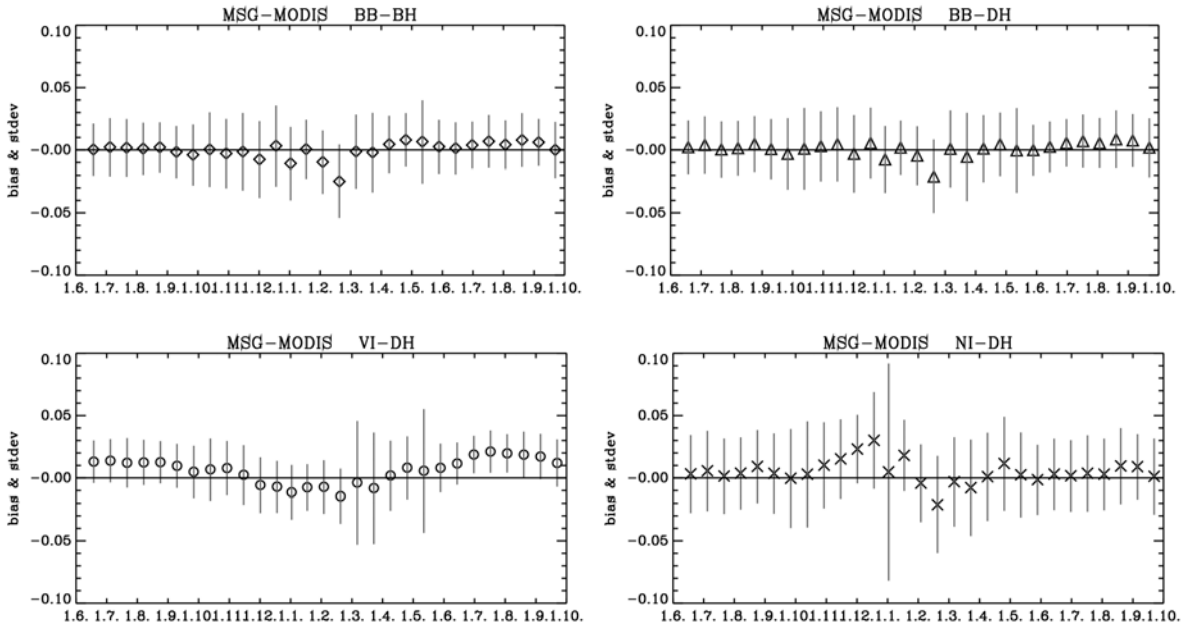


Figure 12: Temporal evolution (June 2005 to September 2006) of the bias and standard deviation between LSA SAF and MODIS broad-band albedo results for Europe. The position of the symbols in the graphs indicates the bias, and the length of the bars (from the centre to each end) corresponds to the standard deviation. Top Left: Total short-wave bi-hemispherical. Top Right: Total short-wave directional-hemispherical. Bottom Left: Visible directional-hemispherical. Bottom Right: Near infrared directional-hemispherical.

4.2 Known Problems and Limitations

- The albedo product time series may still contain spurious variability on short time scales which is caused by atmospheric effects (mainly due to aerosols) that are not yet adequately taken into account.

- Around winter solstice the product quality at high Northern latitudes is reduced due to the low solar elevation angles. In mountainous areas during this period artefacts on the pixel scale caused by shadows can also occur.

- Solar eclipses are not taken into account and can perturb the product quality.

- The data generated before the formal release of the product in September 2005 should not be used. Due to system malfunctions the products generated in September/October 2006 are partially corrupted.

4.3 Comparison between D01 and D10 products

The D10 is a composite product expanding over a typical 30-day and which is derived from the daily (D01) albedo products. The D10 product is produced every 10 days. The reliability of this climatologic product is verified through a comparison with the daily (D01) product over 2 contrasted sites located in Namibia (Gobabeb) and Estonia (Toravere). The validation is supported by the availability of time series of tower flux measurements of broadband albedo collected over these 2 sampled sites in 2009 (Figure 13).

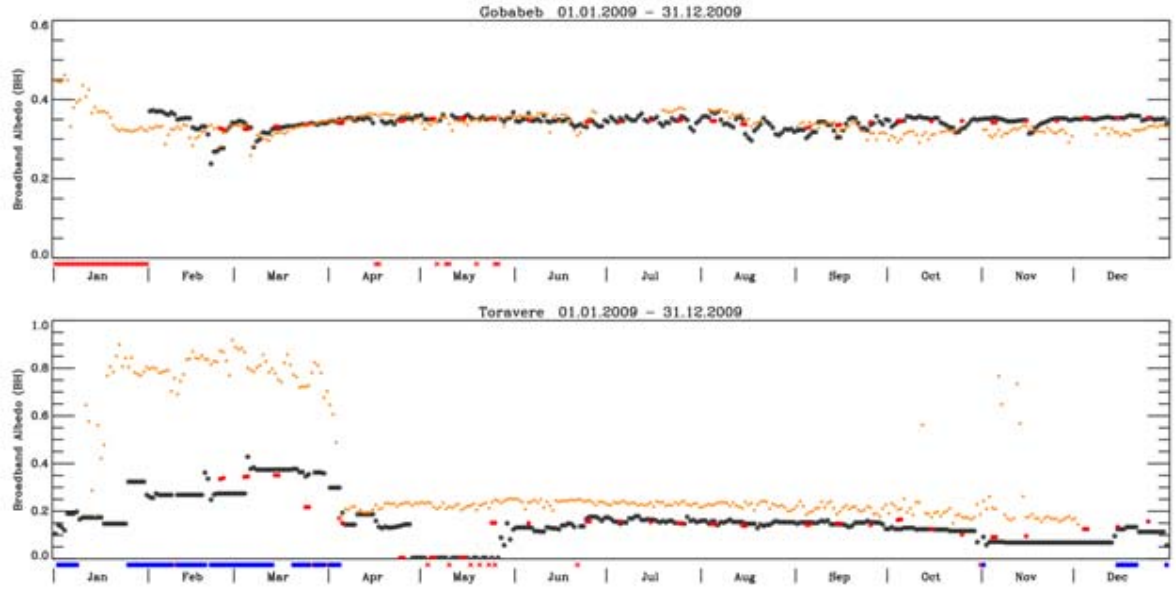


Figure 13: Time series of broadband albedo acquired in 2009 over 2 confident sites (Top: Gobabeb; Bottom: Toravere). Ground measurements (orange). D01 (black). D10 (red). Red/blue dots on the X-axis indicate missing data.

.

5 References

Barnsley M.J., Strahler A.H., Morris K.P., and J.P. Muller, 1994, *Sampling the surface bidirectional reflectance distribution function (BRDF): Evaluation of current and future satellite sensors*, Remote Sensing Reviews, 8, 271-311.

Berthelot B., Dedieu G., Cabot F., and S. Adam, 1994, *Estimation of surface reflectances and vegetation index using NOAA/AVHRR: Methods and results at global scale*, Communications for the 6th International Symposium on Physical Measurements and Signatures in Remote Sensing, Val d'Isère, France, Jan. 17-21, 1994.

Berthelot B., 2001, *Coefficients SMAC pour MSG*, Noveltis Internal Report NOV-3066-NT-834.

Briegleb B.P., P. Minnis, V. Ramanathan, and E. Harrison, 1986, *Comparison of Regional Clear-Sky Albedos Inferred from Satellite Observations and Model Computations*, Journal of Applied Meteorology, 25, 2, 214-226.

Derrien M., 2002, *Specifications Calibration SEVIRI*, SPEC/MSG/001 v1.3, 2002, Météo-France/CMS.

Dickinson R.E., 1983, *Land surface processes and climate – Surface albedos and energy balance*, Advances in Geophysics, 25, 305-353.

Diner D.J. et al. (16 authors), 1998, *Multi-angle imaging spectro-radiometer (MISR) instrument description and experiment overview*, IEEE Transactions on Geoscience and Remote Sensing, 36, 1072-1087.

Ferranti, L. e P. Viterbo, 2006: The European Summer of 2003: Sensitivity of Soil Water Initial Conditions. *J. Climate*, 19, 3659-3680.

Geiger B., Hagolle O., and P. Bicheron, 2005, *CYCLOPES-Project: Directional Normalisation, Algorithm Theoretical Basis Document,* version 2.0.

Hagolle O., Lobo A., Maisongrande P., Cabot F., Duchemin B., and de Pereyra A., 2004, *Quality assessment and improvement of temporally composited products of remotely sensed imagery by combination of VEGETATION 1 & 2 images,* Remote Sensing of Environment, 94, 172-186.

Hook S. J., 1998, ASTER Spectal Library. http://speclib.jpl.nasa.gov

Hu B., Lucht W., Li X., and A.H. Strahler, 1997, *Validation of kernel-driven models for global modeling of bidirectional reflectance*, Remote Sensing of Environment, 62, 201-214.

Justice C.O. et al. (23 authors), 1998, *The Moderate Resolution Imaging Spectroradiometer (MODIS): Land remote sensing for global change research*, IEEE Transactions on Geoscience and Remote Sensing, 36, 1228-1249.

van Leeuwen W. and J.-L. Roujean, 2002, *Land surface albedo from the synergistic use of polar (EPS) and geo-stationary (MSG) observing systems. An assessment of physical uncertainties*, Remote Sensing of Environment, 81, 273-289.

Leroy M., Deuzé J.L., Bréon F.M., Hautecoeur O., Herman M., Buriez J.C., Tanré D., Bouffiès S., Chazette P., and J.L. Roujean, 1997, *Retrieval of atmospheric properties and surface bidirectional reflectances over the land from POLDER/ADEOS*, Journal of Geophysical Research, 102(D14), 17023-17037.

Li X., Gao F., Wang J., and A. Strahler, 2001, *A priori knowledge accumulation and its application to linear BRDF model inversion*, Journal of Geophysical Research, 106(D11), 11925-11935.

Lucht W. and P. Lewis, 2000, *Theoretical noise sensitivity of BRDF and albedo retrieval from the EOS-MODIS and MISR sensors with respect to angular sampling*, International Journal of Remote Sensing, 21, 1, 81-98.

Lucht W. and J.L. Roujean, 2000, *Considerations in the parametric modeling of BRDF and albedo from multiangular satellite sensor observations*, Remote Sensing Reviews, 18, 343-379.

Mitchell, K., et al., 2004: The multi-institution North American Land Data Assimilation System NLDAS: Utilizing multiple GCIP products and partners in a continental distributed hydrological modeling system, *J. Geophys. Res.*, 109, doi:10.1029/2003JD003823.

Pinty B., Roveda F., Verstraete M.M., Gobron N., Govaerts Y., Martonchik J.V., Diner D.J., and R. A. Kahn, 2000a, *Surface albedo retrieval from Meteosat. 1. Theory*, Journal of Geophysical Research, 105(D14), 18099-18112

Pinty B., Roveda F., Verstraete M.M., Gobron N., Govaerts Y., Martonchik J.V., Diner D.J., and R. A. Kahn, 2000b, *Surface albedo retrieval from Meteosat. 2. Applications*, Journal of Geophysical Research, 105(D14), 18113-18134

Pokrovsky I.O., Pokrovsky O.M., and J.-L. Roujean, 2003, *Development of an operational procedure to estimate surface albedo from the SEVIRI/MSG observing*

system in using POLDER BRDF measurements, Remote Sensing of Environment, 87, 198-242.

Press W. H., Teukolsky S. A., Vetterling W. T., and B. P. Flannery, 1992, *Numerical Recipes in Fortran*, Cambridge University Press.

Rahman H. and G. Dedieu, 1994, *SMAC: A simplified method for the atmospheric correction of satellite measurements in the solar spectrum*, International Journal of Remote Sensing, 15, 1, 123-143.

Roujean J.-L., M. Leroy, and P.-Y. Deschamps, 1992, *A bidirectional reflectance model of the Earth's surface for the correction of remote sensing data*, Journal of Geophysical Research, 97(D18), 20455-20468.

Samain O., 2005, *Fusion multi-capteurs de données satellitaires optiques pour la détermination de variables biophysiques de surface*, Ph.D.-Thesis, Université Paul Sabatier, Toulouse.

Schmetz, J., P. Pili, S. Tjemkes, D. Just, J. Kerkman, S. Rota, and A. Ratier (2002), An introduction to Meteosat Second Generation (MSG), *Bull. Amer. Meteor. Soc*., *83*, 977-992.

Sellers P.J., Mintz Y., Sud Y.C. and A. Duldres, 1986, *Simple Biosphere (SiB) Model for Use Within General Circulation Models*, J. Atm. Sci., 43, 505-531.

Strahler A.H., 1994, *Vegetation canopy reflectance modeling - Recent developments and remote sensing perspectives,* Proceedings of the 6th International Symposium on Physical Measurements and Signatures in Remote Sensing, 593-600.

Strahler A.H., Muller J.P. et al. (21 authors), 1999, *MODIS BRDF/Albedo Product: Algorithm Theoretical Basis Document,* version 5.0.

Trigo, I. F., C. C. DaCamara, P. Viterbo, J.-L. Roujean, F. Olesen, C. Barroso, F. Camacho-de-Coca, D. Carrer, S. C. Freitas, J. García-Haro, B. Geiger, F. Gellens-Meulenberghs, N. Ghilain, J. Meliá, L. Pessanha, N. Siljamo, A Arboleda (2010), The Satellite Application Facility on Land Surface Analysis, *Int. J. Remote Sens*., in press.

Verhoef W., 1984, *Light scattering by leaf layers with application to canopy reflectance modeling, the SAIL model*, Remote Sensing of Environment, 16, 125-141.

Wanner W., Li X., and A.H. Strahler, 1995, *On the derivation of kernels for kernel-driven models of bidirectional reflectance*, Journal of Geophysical Research, 100(D10), 21077-21090.

Wanner W., Strahler A., Hu B., Lewis P., Muller J.-P., Li X., Barker-Schaaf C., and M. Barnsley, 1997, *Global retrieval of BRDF and albedo over land from EOS MODIS and MISR data: Theory and algorithm*, Journal of Geophysical Research, 102(D14), 17143-17161.

Appendix A. Developers

The development and implementation have been carried out under the responsibility of the Centre National de Recherches Météorologiques (CNRM) de Météo-France (MF).

Authors: Bernhard Geiger, Dominique Carrer, Laurent Franchistéguy, Jean-Louis Roujean, and Catherine Meurey

Appendix B. Glossary

AL:	Land Surface Albedo Product
AVHRR:	Advanced Very High Resolution Radiometer
BRDF:	Bi-directional Reflectance Distribution Function
CNRM:	Centre National de Recherches Météorologiques
CMa:	Cloud Mask product developed by the NWC-SAF
cwv:	column water vapour
CYCLOPES:	Carbon Cycle and Change in Land Observational Products from an Ensemble of Satellites
ECMWF:	European Centre for Medium-Range Weather Forecast
EPS:	EUMETSAT Polar System
EUMETSAT:	European Meteorological Satellite Organisation
HDF:	Hierarchical Data Format
IM:	Instituto de Meteorologia (Portugal)
NIR:	Near Infrared Radiation
LSA:	Land Surface Analysis
METEOSAT:	Geostationary Meteorological Satellite
METOP:	Meteorological Operational polar satellites of EUMETSAT
MISR:	Multi-Angle Imaging Spectra-Radiometer
MF:	Météo-France
MODIS:	Moderate-Resolution Imaging Spectro-Radiometer
MSG:	Meteosat Second Generation
NOAA:	National Oceanic and Atmospheric Administration (USA)
NWC:	NowCasting
NWP:	Numerical Weather Prediction
POLDER:	POLarization and Directionality of Earth Reflectance
SAF:	Satellite Application Facility
SeaWifs:	Sea-Viewing Wide-Field Sensor
SEVIRI:	Spinning Enhanced Visible and Infrared Imager
SMAC:	Simplified Method for the Atmospheric Correction
TOC:	Top of Canopy
TOA:	Top of Atmosphere
URD:	User Requirements Document

Appendix C. HDF5-Attributes

The set of general attributes common for all LSA SAF files and their possible values are described in the table below.

Table 11 General HDF5 attributes.

Attribute	Description	Data Type	Allowed Values
SAF	SAF package	String	LSA
CENTRE	Institution (generating/disseminating data)	String	MF
ARCHIVE_FACILITY	Centre where the data is archived	String	IM-PT
PRODUCT	Defines the name of the product	String	AL-C?, or ALBEDO
PARENT_PRODUCT_NAME	Array of up to 4 product names, upon which the product is based	String Array(4)	AL-C?-K012, AL-C?-CK, LAT or AL-C1, AL-C2, AL-C3
SPECTRAL_CHANNEL_ID	Channel Identification (1 bit per channel, where LSB is HRV and MSB is IR13.4; values are 0 if not used, 1 if used.)	Integer	14
PRODUCT_ALGORITHM_VERSION	Version of the Algorithm that produced the product	String	5.1
CLOUD_COVERAGE	Indicator of the cloud coverage in the product	String	NWC-CMa
OVERALL_QUALITY_FLAG	Overall quality flag for the product	String	OK or NOK
ASSOCIATED_QUALITY_INFORMATION	Several miscellaneous quality indicators for the product	String	-
REGION_NAME	Processed Region Name	String	Euro, NAfr, SAfr, or SAme.
COMPRESSION	Compression Flag	Integer	0 – Uncompressed 1 – Compressed
FIELD_TYPE	Data filed type	String	Product
FORECAST_STEP	Forecast Step in Hours	Integer	0
NC	Number of columns	Integer	Depends on Region
NL	Number of lines	Integer	Depends on Region
NB_PARAMETERS	Number of datasets	Integer	5 or 9
NOMINAL_PRODUCT_TIME	Production Time	String	YYMMDDhhmmss

Attribute	Description	Data Type	Allowed Values
SATELLITE	Platform identifier (mission and spacecraft the product originated from)	String Array(10)	MSG1 or MSG2
INSTRUMENT_ID	Instrument which acquired the product or data used by the product	String Array(10)	SEVI
INSTRUMENT_MODE	Scanning mode of the instrument at the time of the acquisition.Satellite Identification	String	STATIC_VIEW
IMAGE_ACQUISITION_TIME	Image Acquisition Time (SEVIRI 1.5 Images)	String	YYMMDD
ORBIT_TYPE	Coverage of the product (only for EPS)	String	GEO
PROJECTION_NAME	Projection name and sub-satellite point	String	GEOS(+000.0)
NOMINAL_LONG	Satellite Nominal Longitude	Real	as in Level 1.5 data
NOMINAL_LAT	Satellite Nominal Latitude	Real	as in Level 1.5 data
CFAC	Column Scaling Factor (SEVIRI 1.5 Images)	Integer	as in Level 1.5 data
LFAC	Line Scaling Factor (SEVIRI 1.5 Images)	Integer	as in Level 1.5 data
COFF	Column Offset (SEVIRI 1.5 Images)	Integer	Depends on Region
LOFF	Line Offset (SEVIRI 1.5 Images)	Integer	Depends on Region
START_ORBIT_NUMBER	First of two orbit numbers in the EPS product, valid at the starting of the sensing, i.e, at the beginning of a dump	Integer	0
END_ORBIT_NUMBER	Final of the orbit numbers in the EPS product, valid at the ascending node crossing, i.e. towards the end of a dump	Integer	0
SUB_SATELLITE_POINT_START_LAT	Latitude of sub-satellite at start of acquisition	Real	0.0
SUB_SATELLITE_POINT_START_LON	Longitude of sub-satellite at start of acquisition	Real	0.0
SUB_SATELLITE_POINT_END_LAT	Latitude of sub-satellite at end of acquisition	Real	0.0
SUB_SATELLITE_POINT_END_LON	Longitude of sub-satellite at end of acquisition	Real	0.0
SENSING_START_TIME	UTC date & time at acquisitions start of the product	String	-

Attribute	Description	Data Type	Allowed Values
SENSING_END_TIME	UTC date & time at acquisition end of the product	String	-
PIXEL_SIZE	For image products, size of pixel at nadir. For meteorological products resolution/accuracy	String	3.1km
GRANULE_TYPE	Type description of the item	String	DP
PROCESSING_LEVEL	Processing Level Applied for generation of the product	String	3
PRODUCT_TYPE	Abbreviation name for the product type rather product category	String	LSA AL-C? or LSA ALBEDO
PRODUCT_ACTUAL_SIZE	Actual size of the product	String	9966159 or 18824967
PROCESSING_MODE	Processing mode for generation of the product	String	N, B, R, or V
DISPOSITION_FLAG	Disposition status indicator of the product, as set by the UMARF operator	String	O, T, or C
TIME_RANGE	Temporal Resolution	String	frequency: daily or frequency: ?-days
STATISTIC_TYPE	Statistic Type	String	recursive, timescale: ?days or composition period: ?days

LSB – Lower Significant Bit
MSB – Most Significant Bit
YY - Year; MM-Month; DD – Day; hh – Hour; mm – Minute; ss – Second
String => Character (len=80)
Integer => Integer (kind=4)
Real => Real (kind=8)

The attributes for each dataset of the HDF5-files are described in the following table.

Table 12 Dataset attributes.

Attribute	Description	Data Type	Value for Albedo Datasets	Value for Albedo Error Datasets	Value for Q-Flag Datasets	Value for Age Datasets
CLASS	Dataset type	String	Data	Data	Data	Data
PRODUCT	Defines the name of the product	String	Name of albedo variant	“Error of” + Name of albedo variant	Q-Flag	Z_Age
PRODUCT_ID	Product identification accordingly with WMO tables	Integer	84	128	128	128
N_ COLS	Number of columns	Integer	Depends on Region	Depends on Region	Depends on Region	Depends on Region
N_ LINES	Number of lines	Integer	Depends on Region	Depends on Region	Depends on Region	Depends on Region
NB_BYTES	Number of bytes per pixel	Integer	2	2	1	1
SCALING_FACTOR	Scaling factor for the parameter	Real	10000.0	10000.0	1.0	1.0
OFFSET	Offset of the scaling factor	Real	0.0	0.0	0.0	0.0
MISS_VALUE	Missing value	Integer	-1	-1	999	-1
UNITS	Parameter Units	Integer	1	1	N/A	Days
CAL_SLOPE	Calibration Constant	Real	1.0	1.0	1.0	1.0
CAL_OFFSET	Calibration Constant	Real	0.0	0.0	0.0	0.0